Top Yukawa coupling determination at high energy muon collider

Zhen Liu[1], Kun-Feng Lyu,[1] Ishmam Mahbub,[1] and Lian-Tao Wang[2,3,4]

[1]*School of Physics and Astronomy, University of Minnesota, Minneapolis, Minnesota 55455, USA*
[2]*Department of Physics, University of Chicago, Chicago, Illinois 60637, USA*
[3]*Enrico Fermi Institute, University of Chicago, Chicago, Illinois 60637, USA*
[4]*Kavli Institute for Cosmological Physics, University of Chicago, Chicago, Illinois 60637, USA*

The Top Yukawa coupling profoundly influences several core mysteries linked to the electroweak scale and the Higgs boson. We study the feasibility of measuring the Top Yukawa coupling at high energy muon colliders by examining the high energy dynamics of the weak boson fusion to top quark pair processes. A deviation of the Top Yukawa coupling from the Standard Model would lead to a modified $VV \to t\bar{t}$ process, violating unitarity at high energy. Our analysis reveals that utilizing a muon collider with a center-of-mass energy of 10 TeV and an integrated luminosity of 10 ab^{-1} allows us to investigate the Top Yukawa coupling with a precision surpassing 1.5%, more than one order of magnitude better than the precision from $t\bar{t}h$ channel at muon colliders. This precision represents a notable enhancement compared to the anticipated sensitivities of the High-Luminosity LHC (3.4%) and those at muon colliders derived from the $t\bar{t}H$ process.

I. INTRODUCTION

Following the discovery of the Higgs boson in 2012 [1,2], the elucidation of its properties, particularly its interactions with other Standard Model (SM) fields, has become one of the top priorities of particle physics. Substantial efforts at the LHC have focused on quantifying Higgs interactions with fermions, gauge bosons, and self-couplings. Nonetheless, precision measurements at hadron colliders face constraints due to substantial QCD backgrounds. Muon colliders (MuCs) have emerged as an exciting venue for high precision Higgs exploration. Recent research accentuates their potential, combining the precision of lepton colliders with high center-of-mass energies, thereby allowing for exploration at scales of 10 TeV or higher in an environment with low background [3–14]. Admittedly, one inherent challenge for muon colliders is the short lifetime of muons. The high energy physics community is working on tackling the challenges and the research to enable a future muon collider, in particular, through an ionization cooling scheme.

A crucial physics objective for future colliders is the precise measurement of Higgs couplings. The Top Yukawa coupling, one of the least constrained parameters in the SM, holds significance for Higgs research, with its deep connection to the profound puzzle of naturalness and Higgs

vacuum stability. The recent LHC measurement for Top Yukawa is $y_t = 1.16^{+0.24}_{-0.35}$ [15].

This study emphasizes the measurement of the Top Yukawa coupling at muon colliders. The dominance of electroweak gauge boson fusion at muon colliders results from the logarithmic growth of the electroweak parton distribution function (PDF) with energy [5,16–22]. We adopt a factorization approach to compute cross sections, integrating the enhanced collinear splitting with the vector boson hard scattering. Factorization and resummation ensure a cross section devoid of collinear divergences in high energy limits. Our initial assumption only considers a Higgs coupling shift $y_t \to y_t(1 + \delta_{yt})$ through a single Standard Model Effective Theory (SMEFT) operator $\mathcal{O}^t_y = H^\dagger H \bar{Q} \tilde{H} t_R$. Additionally, we examine a scenario involving a heavy singlet vectorlike quark.

The paper is structured as follows: Sec. II introduces our theoretical framework. Section III details various partonic channels. Section IV presents the results, and Sec. V contains our conclusions.

II. THEORETICAL FRAMEWORK

The Top Yukawa coupling can be directly measured from processes with final states containing Higgs boson, such as $ht\bar{t}$. One can also access the Top Yukawa coupling with processes with Higgs boson in the intermediate state but not appearing in the external legs. The scattering amplitude of a process with longitudinal gauge bosons as external states, such as $VV \to t\bar{t}$, could grow with energy if a coupling deviates from the SM. As a result, such an
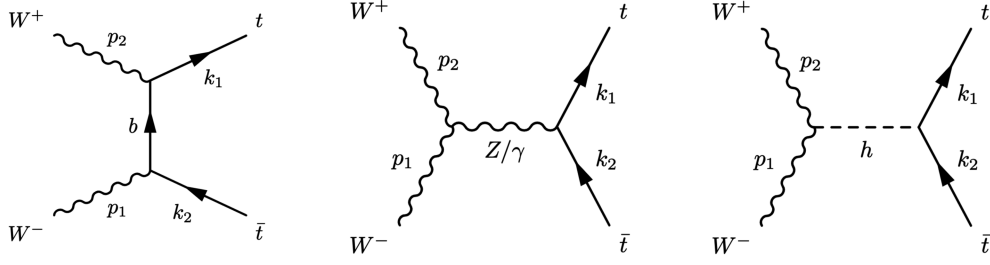
FIG. 1. The Feynman diagrams for the process $W^+W^- \to t\bar{t}$.

amplitude eventually violates unitarity at a high energy scale, implying the breakdown of the low energy description and the appearance of new physics. Similar study on the gauge boson scattering has been carried on in [23–27] to probe the dynamics of electroweak symmetry breaking and various new physics sectors.

In this section, we first examine the effects of the anomalous Top Yuakawa coupling in the $W_L^+W_L^- \to t\bar{t}$ channel and focus on the energy dependence of the scattering amplitude. We then discuss some possible UV models that can generate such Top Yukawa coupling and further discuss the electroweak PDF which would be convoluted with the $VV \to t\bar{t}$ cross section to obtain the total signal rate at muon colliders.

A. Perturbative unitarity in the $W_L^+W_L^- \to t\bar{t}$ process

In this section, we consider the channel $W_L^+W_L^- \to t\bar{t}$ to illustrate the role of perturbative unitarity in the process. Our analysis of $t\bar{t}$ production in muon colliders involves initial state vector boson WW, ZZ, $Z\gamma$, and $\gamma\gamma$, but we choose $W_L^+W_L^- \to t\bar{t}$ as our example here since it is the dominant channel in our analysis. As shown in Fig. 1, the Feynman diagrams for the process can be divided into three categories. The first is the t-channel diagram via the exchange of the b quark. The second is the s-channel diagram mediated by the neutral vector boson, and the last diagram is mediated by the Higgs boson in the s channel. The leading order contribution for the amplitude of the first and second diagrams can be estimated to be $O(E^2/m_W^2)$ by dimensional analysis for $t, \bar{t}$ helicity of $(\pm, \mp)$ and $O(E/m_W)$ for $t, \bar{t}$ helicity of $(\pm, \pm)$. For the case of opposite outgoing helicity of the quarks, once we add the contributions from individual diagrams, the leading $O(E^2/m_W^2)$ behavior of each diagram is canceled through gauge symmetry, leaving a constant term as would be needed for unitarity. While for the case of the same quark helicity, the leading order energy scaling is not eliminated without adding the contribution from the Higgs-mediated diagram. After combining all four diagrams, the energy growth behavior is precisely canceled, and perturbative unitarity in this process is restored. Such a cancellation is expected from the Goldstone boson equivalence theorem. In the high energy limit, we have

$$\mathcal{M}_{W_L^+W_L^- \to t\bar{t}} = \mathcal{M}_{\phi^+\phi^- \to t\bar{t}}\left[1 + O\left(\frac{m_W^2}{E^2}\right)\right]. \quad (1)$$

The amplitude for $\mathcal{M}_{\phi^+\phi^- \to t\bar{t}}$ in SM is at most a constant. Hence, we do not expect unitarity-violating behavior in the $W_L^+W_L^- \to t\bar{t}$ process.

If the Top Yukawa is shifted,

$$y_t \to y_t(1 + \delta_{y_t}), \quad (2)$$

only the amplitude of the Higgs-mediated diagram will be modified from the SM, and one can show that in the high energy limit, the total scattering amplitude is

$$\mathcal{M}(W^+W^- \to t\bar{t}) = \frac{m_t}{v^2}\delta_{y_t}\sqrt{s} \quad \text{for } \sqrt{s} \gg m_t. \quad (3)$$

In order to preserve unitarity, or more precisely, to maintain the validity of a weakly coupled Effective Field Theory (EFT), there must be a cutoff. To estimate this cutoff, we can follow the standard partial wave analysis. The $J = 0$ partial wave amplitude is

$$a_0 = \frac{1}{32\pi}\int_{-1}^{1} d\cos\theta|\mathcal{M}|. \quad (4)$$

Unitarity requires the amplitude $|a_0| \leq 1$. Hence, we obtain the cutoff as (ignoring the constant term)

$$\Lambda_{\mathrm{BSM}} < \frac{16\pi v^2}{m_t\delta_{y_t}}. \quad (5)$$

The current precision on the Top Yukawa coupling y_t is around $\mathcal{O}(10)\%$. Therefore, the cutoff scale is well above the center-of-mass energy of a 10 TeV muon collider. We note that the parametrization in Eq. (2) is (overly) simplified. We can also characterize the deviation in terms of the contribution from new physics. In the following, we describe two approaches to parametrize such contributions.

B. Dimension-six operator

The most straightforward way to express the deviation of the Top Yukawa coupling from the SM is in terms of the higher dimensional operators in SMEFT [28–30],

generated after integrating out heavy new physics [31,32]. One can assume the leading EFT operator is $\mathcal{O}_y^t = (H^\dagger H)\bar{Q}_L \tilde{H} t_R$ with the corresponding Wilson coefficient c_y^t.[1] After electroweak symmetry breaking (EWSB) and combining it with the Top Yukawa coupling term, we get

$$
\mathcal{L} \supset -\left[m_t + \left(\frac{m_t}{v} - \frac{c_y^t v^2}{\sqrt{2}}\right)h - \frac{3c_y^t v}{2\sqrt{2}}h^2 - -\frac{3c_y^t}{2\sqrt{2}}h^3\right]
$$
$$
\times (\bar{t}_L t_R + \bar{t}_R t_L), \tag{6}
$$

in the unitary gauge. After imposing the top pole-mass physical boundary condition, the Top Yukawa coupling is shifted by

$$
\delta_{yt} = -\frac{c_y^t v^3}{\sqrt{2} m_t}. \tag{7}
$$

The additional terms in Eq. (6) are higher dimensional operators describing interactions between the top quark pair and two or three Higgs bosons. Since we are considering the $VV \to t\bar{t}$ process, only the single Higgs coupling would enter the calculations. Beyond the scenario, only the operator O_y^t is turned on, and other operators could also enter the process. Such an assumption, while minimal, may be oversimplifying. In addition to O_y^t, the UV models often generate multiple operators at the same time. Next, we present one simple UV scenario to generate the effective anomalous Yukawa coupling in the IR.

C. Vectorlike quarks

Models with vectorlike quarks (VLQs), as a simple extension of SM, are motivated in a broad class of new physics theories (see, e.g., Refs. [33–35] and references therein). As seen from its name, it is similar to quarks, transforming as a triplet under the $SU(3)_C$ group. Its left- and right-handed components carry the same color and electroweak charge. It is possible to write a mass term independent of the Higgs vacuum expectation value. Therefore, it has a decoupling limit, and it is consistent with the electroweak precision and Higgs precision data. We can exploit its mixing with the third generation quarks to obtain the effective non-SM Yukawa coupling at low energies.

We start from the simple case that the VLQ is an SM electroweak SU(2) singlet [36] and has the same quantum numbers as right-handed top quark, t_R. Denoting the one

---

[1]For simplicity, we consider the c_y^t being real here. One can study consistently defined *CP*-violation effects in detail in differential decays, which will not affect the inclusive rate that we focus on here.

---

flavor VLQ as T, its left- and right-handed components are T_L and T_R. The relevant Lagrangian is

$$
\mathcal{L} \supset i\bar{T}\slashed{D}T - (\lambda_1 \bar{Q}_L \tilde{H} t_R + \lambda_2 \bar{Q}_L \tilde{H} T_R + M_1 \bar{T}_L t_R + M_2 \bar{T}_L T_R). \tag{8}
$$

However, we can always combine t_R and T_R to get a new right-handed quark, which we still denote as T_R. This field redefinition can remove the mass mixing term between T_L and t_R. The resulting Lagrangian is

$$
\mathcal{L} \supset i\bar{T}\slashed{D}T - (\lambda_t \bar{Q}_L \tilde{H} t_R + \lambda_0 \bar{Q}_L \tilde{H} T_R + M_0 \bar{T}_L T_R). \tag{9}
$$

After EWSB, we can write down the mass matrix as follows:

$$
-\mathcal{L} \supset (\bar{t}_L \quad \bar{T}_L)\begin{pmatrix} \lambda_t v/\sqrt{2} & \lambda_0 v/\sqrt{2} \\ 0 & M_0 \end{pmatrix}\begin{pmatrix} t_R \\ T_R \end{pmatrix} + \text{H.c.}
$$
$$
= \bar{F}_L M F_R + \text{H.c.}, \tag{10}
$$

in which we abbreviate the left-handed and right-handed fermions into the column vectors, F_L and F_R, respectively. The mass matrix is denoted as M. Note that for fermions, we need separate transformations for the left- and right-handed components, U_L and U_R, respectively, to diagonalize the mass matrix. We have

$$
U_L M U_R^\dagger = \Lambda = \begin{pmatrix} m_t & \\ & m_T \end{pmatrix} \quad \text{with}
$$
$$
U_{L,R} = \begin{pmatrix} c_{L,R} & s_{L,R} \\ -s_{L,R} & c_{L,R} \end{pmatrix}, \tag{11}
$$

where m_t and the M_T are the physical masses of the top quark and the VLQ. In the mass basis, the Yukawa matrix can be written as

$$
U_L \begin{pmatrix} \lambda_t & \lambda_0 \\ 0 & 0 \end{pmatrix} U_R^\dagger = \frac{\sqrt{2}}{v} U_L \begin{pmatrix} 1 & 0 \\ 0 & 0 \end{pmatrix} U_L^\dagger \Lambda
$$
$$
= \frac{\sqrt{2}}{v} \begin{pmatrix} c_L^2 m_t & -c_L s_L m_T \\ -c_L s_L m_T & s_L^2 m_T \end{pmatrix}. \tag{12}
$$

On the other hand, using the identity $U_L M M^\dagger U_L^\dagger = \Lambda^2$, we can obtain the relative shift for the Top Yukawa coupling,

$$
\delta_{yt} = -s_L^2 = -\frac{(\lambda_t^2 + \lambda_0^2)v^2/2 - m_t^2}{m_T^2 - m_t^2}. \tag{13}
$$

In the limit $m_T \gg m_t$, we have $\delta_{yt} \sim v^2/m_T^2$, as expected from the correction induced by a dimension-6 operator. Moreover, the fermion field rotation would modify the coupling between the top quark and the gauge field. Making the replacement that $t_L \to c_L t_L - s_L T_L$, we get

$$\frac{g}{\sqrt{2}} W_\mu^+ \bar{t}_L \gamma^\mu b_L \to \frac{g}{\sqrt{2}} W_\mu^+ (c_L \bar{t}_L \gamma^\mu b_L - s_L \bar{T}_L \gamma^\mu b_L),$$

$$\frac{g}{\cos\theta_w}\left(\frac{1}{2} - \frac{2}{3}\sin^2\theta_w\right) Z_\mu \bar{t}_L \gamma^\mu t_L \to \frac{g}{\cos\theta_w}\left(\frac{1}{2} - \frac{2}{3}\sin^2\theta_w\right) Z_\mu[c_L^2 \bar{t}_L \gamma^\mu t_L - c_L s_L(\bar{t}_L \gamma^\mu T_L + \bar{T}_L \gamma^\mu t_L) + s_L^2 \bar{T}_L \gamma^\mu T_L],$$

$$\frac{g}{\cos\theta_w}\left(-\frac{2}{3}\sin^2\theta_w\right) Z_\mu \bar{T}_L \gamma^\mu T_L \to \frac{g}{\cos\theta_w}\left(-\frac{2}{3}\sin^2\theta_w\right) Z_\mu[s_L^2 \bar{t}_L \gamma^\mu t_L + c_L s_L(\bar{t}_L \gamma^\mu T_L + \bar{T}_L \gamma^\mu t_L) + c_L^2 \bar{T}_L \gamma^\mu T_L]. \tag{14}$$

Apart from the modified $Zt\bar{t}$ coupling, there are also new off-diagonal couplings of the form $V - T - t$, with V being the charged and neutral gauge bosons. These couplings would modify the electroweak oblique parameters T and S, thus being highly constrained. However, one can always add more vectorlike quarks carrying the same charge as the bottom quark to compensate. Alternatively, we can integrate out the heavy quark and obtain the corresponding matched EFT Lagrangian. At tree level, we get

$$\frac{\lambda_0^2}{M_0^2} \bar{Q}_L \tilde{H} i \slashed{D}(\tilde{H}^\dagger Q_L). \tag{15}$$

After EWSB, this operator leads to the corrections to the top couplings consistent with the mixing effect discussed above at the leading order. The single operator in Eq. (15) can be converted into the operators in Warsaw basis of SMEFT via the equation of motion. We get

$$\frac{\lambda_0^2}{M_0^2}\left[y_t H^\dagger H \bar{Q}_L \tilde{H} t_R + \frac{1}{4} H^\dagger i \overset{\leftrightarrow}{D}_\mu H \bar{Q}_L \gamma^\mu Q_L \right.$$
$$\left. - \frac{1}{4} H^\dagger \sigma^a i \overset{\leftrightarrow}{D}_\mu H \bar{Q}_L \sigma^a \gamma^\mu Q_L \right]. \tag{16}$$

Compared to the coupling modifications discussed in previous sections, apart from the $\mathcal{O}_y^t$ operator, two more operators with correlated coefficients appear and modify the coupling of the charged and neutral current of the third-generation quarks. These correlations have implications when we interpret our results in later sections.

D. Electroweak gauge boson PDFs

Vector boson fusion (VBF) production is one of the most important production channels at high energy colliders. For example, the Higgs boson can be produced by VBF, in addition to the s channel Higgsstrahlung channels at future lepton colliders. As the center-of-mass energy $\sqrt{s}$ increases, the VBF channel becomes more and more important than the s channel. For muon colliders with benchmark $\sqrt{s} = 3$ or 10 TeV, the VBF processes dominate the others for Higgs production. In many cases, a high energy muon collider can be considered a gauge boson collider; the virtual gauge bosons split off the incoming

muon and antimuon beams, then participate in hard scatterings.

There are a couple of challenges in computing the VBF process accurately at high energy colliders. Splitting a muon into a virtual gauge boson plus remnant lepton is highly forward at high energies, and complexities arise for massive gauge bosons. One useful approximation is to treat the nearly on-shell gauge boson as the parton within the incoming muon. Analogous to the proton case, which can be seen as the collection of separate partons in the QCD perturbative energy scale, the total collision cross section is the sum of the convoluted partonic cross section with the parton distribution function. A factorization procedure similar to hadron collisions can be applied here. The full VBF process can be decomposed into the muon splitting part and the gauge boson scattering subprocess. One can derive the PDF for the virtual gauge bosons through the splitting function. Theoretically, it requires solving the Dokshitzer-Gribov-Lipatov-Altarelli-Parisi equation and matching between the massless splitting and massive gauge bosons. The matching can only be meaningfully done with higher order calculation information, which is beyond the scope of this study. The gauge boson scattering subprocesses can be convoluted with the PDF to obtain the cross section. The total cross section can be expressed as

$$\sigma(\mu^+\mu^- \to F + X) = \int_{\tau_{\min}}^{\tau_{\max}} d\tau \sum_{ij} \frac{\mathcal{L}_{ij}}{d\tau} \hat{\sigma}(ij \to F), \tag{17}$$

where X refers to the collinear remnant partons, F stands for the collection of the final state particles from the hard scattering, and i, j label the intermediate virtual gauge bosons. $\tau = \hat{s}/s$ is the fraction of the partonic center-of-mass energy. The parton luminosity function is defined as

$$\frac{d\mathcal{L}_{ij}}{d\tau} = \frac{1}{1 + \delta_{ij}} \int_\tau^1 \frac{d\xi}{\xi}\left[f_i(\xi, \mu_f) f_j\left(\frac{\tau}{\xi}, \mu_f\right) + i \leftrightarrow j\right], \tag{18}$$

in which $f_i(\xi, \mu_f)$ is the PDF for the parton i carrying a fraction of the longitudinal momentum of the incoming muon at the factorization scale μ_f. In the following computation, we set both the factorization scale μ_f and the renormalization scale equal to $\sqrt{\hat{s}}/2$ [18].

The photon PDF is the largest among all gauge bosons due to its huge flux starting from a low energy scale. However, photon-initiated channels make little contribution to the signal part of our analysis which comes from the Higgs exchange diagram. Our main signal channel is from the longitudinal gauge boson initial states, especially $W_L^+ W_L^- \to t\bar{t}$. The longitudinal gauge boson (W_L, Z_L) PDF has no scale dependence at the leading order [37–39], which can be seen as the remnant from the electroweak symmetry breaking. The suppression from the longitudinal gauge boson PDF can be compensated by the large partonic cross section. These features are apparent in Sec. III and key to our sensitivity analysis of the deviation of Top Yukawa coupling.

III. RELEVANT CHANNELS AT MUON COLLIDER

At a high energy muon collider, the primary production channel of top quark pairs is from the VBF process. In this section, we compute the SM partonic cross sections for the processes $VV \to t\bar{t}$ and then present the results after convolution with the muon PDF. FEYNCALC[40] was first used to calculate the helicity amplitude and the cross sections. We then modify the vertices in the SM Universal FeynRules Output model files within MADGRAPH5_AMC@NLO [41,42] as a cross-check. The gauge boson PDF is computed at the truncated to leading logarithmic order as done in [5].

A. Polarized partonic cross section

We first present the SM predictions of the partonic cross sections in Fig. 2, where all the possible initial polarization states of the vector bosons are separately shown for the range of center-of-mass energies from the $t\bar{t}$ threshold to 10 TeV. First, let us look at the WW initial states, the most dominant $t\bar{t}$ production channel. The figure shows that the primary channel is the one in which both incoming $W^\pm$ are longitudinally polarized. The subdominant contribution to the cross section occurs for right-handed W^- with longitudinal W^+ as well as the CP-conjugated combination. In the high energy regime, we observe from the figure that the cross sections of the channels with initial polarization of (W^+, W^-) are $(0,0)$, $(0,+)$, $(-,0)$, $(-,+)(+,-)$ scale as $\hat{s}^{-1}$ and the cross sections of the four other channels scale as $\hat{s}^{-2}$. Therefore, the amplitude squared term does not scale for $(0,0)$, $(0,+)$, $(-,0)$, $(-,+)(+,-)$ and for $(+,0)$, $(0,-)$, $(-,-)$, $(+,+)$ scales as $\hat{s}^{-1}$.

To illustrate the scaling mentioned, we show the explicit $\hat{s}$ dependence of the amplitude squared term of all possible helicity configurations for the $W^+(h_i) + W^-(h_j) \to t(h_k) + \bar{t}(h_l)$ processes in Table I, where the helicity of the particle is shown in the brackets. Here, h_i, h_j can take the value of 1, 0, or -1 while h_k and h_l can be $\pm 1/2$ (labeled as $\pm$ in the table for brevity). The tree-level helicity amplitudes are invariant under the CP transformation,
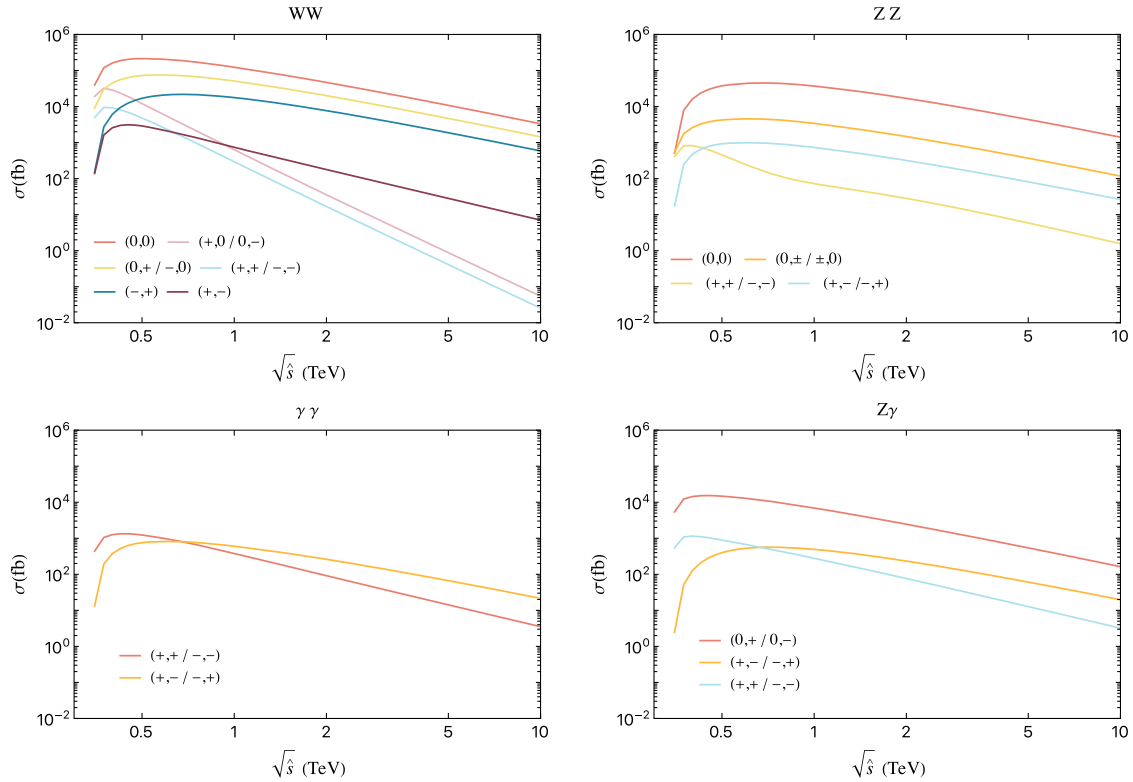

FIG. 2. The SM partonic cross section for $VV \to t\bar{t}$ as a function of the center-of-mass energy $\sqrt{\hat{s}}$ with different initial helicities states.

TABLE I. The high energy $\hat{s}$ scaling of the squared amplitude for $W^+W^- \to t\bar{t}$ where helicities of the outgoing top quarks and incoming W bosons are explicitly shown. Here, we have ignored the potential additional logarithmic dependence. For the fermion helicities, we use $\pm$ to denote their helicity.

		$(t, \bar{t})$			
W^+	W^-	$(+,+)$	$(-,+)$	$(+,-)$	$(-,-)$
0	0	$\hat{s}^{-1}$	$\hat{s}^0$	$\hat{s}^0$	$\hat{s}^{-1}$
$+$	0	$\hat{s}^{-2}$	$\hat{s}^{-1}$	$\hat{s}^{-1}$	$\hat{s}^{-2}$
$-$	0	$\hat{s}^{-2}$	$\hat{s}^{-1}$	$\hat{s}^{-1}$	$\hat{s}^0$
0	$+$	$\hat{s}^0$	$\hat{s}^{-1}$	$\hat{s}^{-1}$	$\hat{s}^{-2}$
$+$	$+$	$\hat{s}^{-1}$	$\hat{s}^{-2}$	$\hat{s}^{-2}$	$\hat{s}^{-3}$
$-$	$+$	$\hat{s}^{-1}$	$\hat{s}^0$	$\hat{s}^{-2}$	$\hat{s}^{-1}$
0	$-$	$\hat{s}^{-2}$	$\hat{s}^{-1}$	$\hat{s}^{-1}$	$\hat{s}^{-2}$
$+$	$-$	$\hat{s}^{-1}$	$\hat{s}^0$	$\hat{s}^{-2}$	$\hat{s}^{-1}$
$-$	$-$	$\hat{s}^{-3}$	$\hat{s}^{-2}$	$\hat{s}^{-2}$	$\hat{s}^{-1}$

$$W^+(h_i) \to W^-(-h_i), \qquad W^-(h_j) \to W^+(-h_j),$$
$$t(h_k) \to \bar{t}(-h_k), \qquad \bar{t}(h_l) \to t(-h_l), \tag{19}$$

which is manifest in the table. For example, if one compares the third and fourth row, $[W^+(-), W^-(0)]$ is transformed to $[W^+(0), W^-(+)]$, and the $\hat{s}$ power is indeed swapped under the CP transformation of the top quark pairs.

We now focus on the scaling of helicity amplitude for $W_L^+ W_L^- \to t\bar{t}$ due to its significance as the Standard Model background as well as the source of the signal.[2] Let us first consider $t, \bar{t}$ helicity $(\pm, \pm)$. For the Top Yukawa coupling we are probing, this channel is the largest source of the signal in our analysis due to the Higgs exchange diagram. Each individual diagram for this helicity scales as $\sqrt{\hat{s}}$ as seen from Eqs. (A14) to (A17) and Eqs. (A26) to (A29) in the high energy limit. Once we add all four diagrams, the leading terms cancels, and in SM, the amplitude scales as $1/\sqrt{\hat{s}}$ which is the next leading order term in all these amplitudes. Note that the signal comes only from the Higgs diagram scaling as $\sqrt{\hat{s}}$, and so its interference with SM therefore does not scale. We elaborate interference and relevant scaling in Sec. IV A.

The leading contribution of $W_L^+ W_L^- \to t\bar{t}$ comes from the final quark helicity $t(+)\bar{t}(-)$, and so, we now focus on $t, \bar{t}$ helicity $(\pm, \mp)$ to understand their behavior. As shown by the helicity amplitude in Appendix A, the amplitudes of the processes with final quarks helicities $(-, +)$ or $(+, -)$ approach a constant in the high energy limit given by

---

[2]$t\bar{t}$ can also be produced through the s-channel process, but it is by far subdominant at high energy muon colliders and easily distinguishable from the signal process considered here due to its energetic top quark jet, high invariant mass, and low rapidity of the $t\bar{t}$ system.

$$\mathcal{M}(W_L^+ W_L^- \to t(+)\bar{t}(-)) = -\frac{2m_t^2}{v^2}\cot\frac{\theta}{2} + \frac{g^2}{3}\sin\theta + \mathcal{O}(1/\hat{s}), \tag{20}$$

$$\mathcal{M}(W_L^+ W_L^- \to t(-)\bar{t}(+)) = \frac{3g^2 + g'^2}{12}\sin\theta + \mathcal{O}(1/\hat{s}), \tag{21}$$

where θ is the angle between W^+ and t in the partonic center-of-mass frame. The leading order behavior of these amplitudes can be understood from the perspective of the Goldstone boson equivalence theorem and from the process $\phi^+\phi^- \to t\bar{t}$. Let us first consider $\phi^+\phi^- \to t(+)\bar{t}(-)$. At leading order, the s-channel process has contribution only from the U(1) field B_μ exchange and no contribution from the $SU(2)_L$ field, which will be of order $O(m_t/\sqrt{\hat{s}})$ for this helicity configuration. The s-channel B_μ diagram is proportional to g'^2 and the Wigner function $d_{0,1}^1 = \sin\theta/\sqrt{2}$. The process also has a t-channel contribution from b-quark exchange which comes from terms in Lagrangian of the form $y_t \bar{b}_L t_R \phi^-$ and its Hermitian conjugate. This explains why in Eq. (20) we observe t-channel behavior proportional to y_t^2. Now, let us consider the channel $\phi^+\phi^- \to t(-)\bar{t}(+)$. In the leading order, the s-channel diagram is mediated by $SU(2)_L$ charge neutral vector boson W_μ^3 with coupling g and U(1) field B_μ with coupling g'. Since we assume $y_b = 0$ in our calculation, the leading order t-channel contribution is of order $\mathcal{O}(m_t/\sqrt{\hat{s}})$ and explains the absence of t-channel behavior in Eq. (21). Due to a t-channel enhancement which is absent in other channels in the leading order, $W_L^+ W_L^- \to t(+)\bar{t}(-)$ dominates top quark pair production from W bosons and serves as the largest SM backgrounds in our analysis.

Furthermore, we numerically compute the amplitude of this channel by decomposing the top current into left-handed current and right-handed current parts separately. Explicitly, each s-channel diagram can be decomposed into the two subdiagrams with $\bar{t}_L \gamma^\mu t_L V_\mu$ and $\bar{t}_R \gamma^\mu t_R V_\mu$ with V being either photon or the neutral Z boson. The t-channel diagram only contains the left-handed current $\bar{t}_L \gamma^\mu b_L$ plus its conjugation $\bar{b}_L \gamma^\mu t_L$. It turns out that the summation of the left-handed current consisting of the $\bar{t}_L \gamma^\mu t_L$ part from the s-channel diagram and the t-channel diagram dominates over the summation of the right-handed current part $\bar{t}_R \gamma^\mu t_R$ from the s-channel diagrams. This can be understood as follows. First, in the $t(+)\bar{t}(-)$ final helicity state, the Higgs diagram does not contribute, and the t-channel diagram only contains the left-handed current. In the high energy limit, the s-channel diagram exchanging Z/γ bosons can be treated as restoring into W_μ^3 field because the W boson pairs can only interact with W_μ^3 via the non-Abelian self-interaction, while the W_μ^3 field can only couple to left-handed current. The right-handed current can be only from the finite Z boson mass effect finally manifested by the g'^2
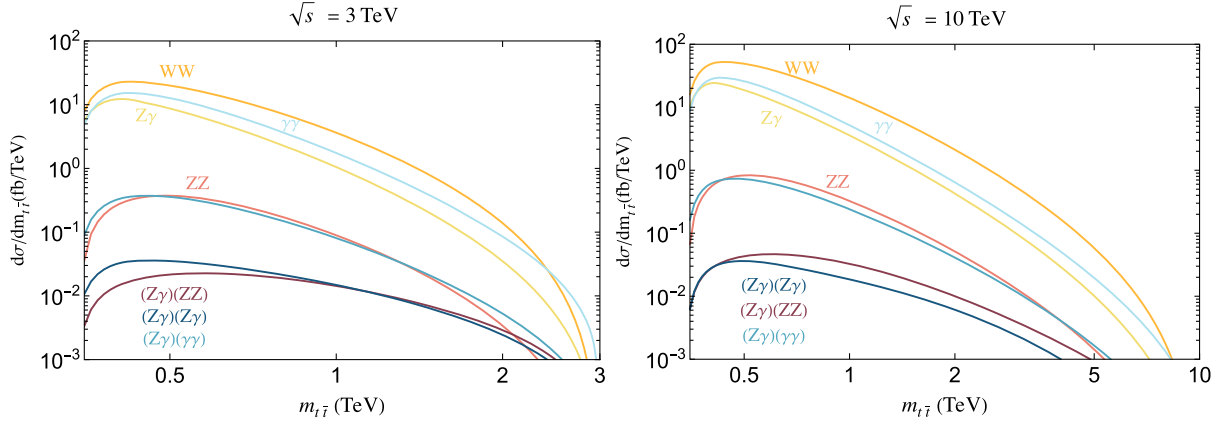
FIG. 3.   The differential distribution for $\mu^+\mu^- \to t\bar{t} + X$ versus the invariant mass $m_{\bar{t}t}$ at a 3 TeV and a 10 TeV MuC.

terms. Such behavior has a significant impact on the VLQ model, which is discussed later on.

For ZZ-fusion channels, the partonic cross section is invariant under the CP transformation and the exchange of initial particle states. Consequently, only four distinct behaviors exist for all possible initial Z boson helicity combinations. Longitudinally polarized Z boson states also dominate the partonic cross section. The subdominant channels consist of one longitudinal polarized Z boson plus the other transverse polarized Z boson. Both t-channel and u-channel diagrams are possible, resulting in both forward and backward enhancement of the differential distribution. This could also be understood because the top quark exchange is symmetric with respect to $\theta = \pi/2$. This contrasts with the WW-fusion case where the t-channel diagram exchanging the b quark prefers the forward direction, and there is no u-channel diagram. For production processes starting from transverse helicity modes, the cross section from the opposite helicity initial state is larger than that of the same helicity.

For the diphoton-initiated processes, there are only two distinct combinations, with either the same or opposite helicities of the photons. One can see that the opposite-helicity case (orange curve) is larger than the same-helicity case (red curve) in the high energy limit. The same-helicity process scales as $\hat{s}^{-1}$ asymptotically while the opposite-helicity process scales as $\hat{s}^{-1} \log \hat{s}$. A similar pattern also shows up in the $Z\gamma$ partonic cross section. It should be emphasized that the photon PDF from muon is around one order smaller than that from the electron at the same factorization scale, due to the two orders difference in the muon and electron mass. This results in a decreased signal rate of the diphoton initiated process at a muon collider.

B. Convolution with PDFs

Having computed the partonic cross section for all possible polarizations of the gauge boson, the next step is to convolute them with the electroweak gauge boson

PDFs. We work with two benchmarks of the center-of-mass energies for the future muon collider: one is $\sqrt{s} = 3$ TeV with an integrated luminosity of $1 \ ab^{-1}$ and the other one with $\sqrt{s} = 10$ TeV with an integrated luminosity of $10 \ ab^{-1}$. In this section, we first present the differential distribution with the invariant mass of the top quark pair in Fig. 3. The orders of $t\bar{t}$ cross section contributions are WW, $\gamma\gamma$, $Z\gamma$, and ZZ initial states. As we have seen in Fig. 2, the partonic cross section of WW is over two orders larger than that of $\gamma\gamma$ although the photon PDF is larger than W boson. Due to the smallness of the Z boson PDF, the ZZ-fusion channel is suppressed while $Z\gamma$ sits in between. Beyond the simple PDF treatment, we also evaluate the importance of the interference effects between different electroweak gauge bosons. After all, the PDF treatment is a quasi-real approximation of the intermediate states, which are fully interfering. From the view of the full $2 \to 4$ process $\mu^+\mu^- \to \mu^+\mu^- t\bar{t}$, the intermediate off-shell gauge boson can be either the Z boson or the photon. One needs to first sum up the amplitudes of both processes before squaring them, namely,

$$\mathcal{M} = \sum_{i,j} \mathcal{M}_{V_{+,i}V_{-,j}} = \mathcal{M}_{ZZ} + \mathcal{M}_{\gamma\gamma} + \mathcal{M}_{Z\gamma} + \mathcal{M}_{\gamma Z,} \quad (22)$$

where we denote V_+ as the neutral gauge boson radiated off μ^+ and V_- from μ^-. After squaring, multiple interference terms should be handled carefully. Remembering that in computing the gauge boson PDF, there is the term $f_{Z\gamma}$ which accounts for the mixing from the splitting amplitude $\mathcal{M}^{\text{split}}_{\mu \to \mu\gamma}$ and $\mathcal{M}^{\text{split}}_{\mu \to \mu Z}$. Hence, the total cross section for $\mu^+\mu^- \to \mu^+\mu^- t\bar{t}$ should be

$$\sigma \sim \sum \int dx_1 dx_2 f_{i_- j_-}(x_1) f_{i_+ j_+}(x_2) \mathcal{M}_{i_- i_+} \mathcal{M}^*_{j_- j_+}. \quad (23)$$

For example, if $i_- = j_- = \gamma$, $f_{i_- j_-}(x)$ equals to $f_\gamma(x)$. The case of $i_- \neq j_-$ corresponds to $f_{Z\gamma}$ function. We use the brackets to enclose $Z\gamma$ in Fig. 3 to show their contributions.
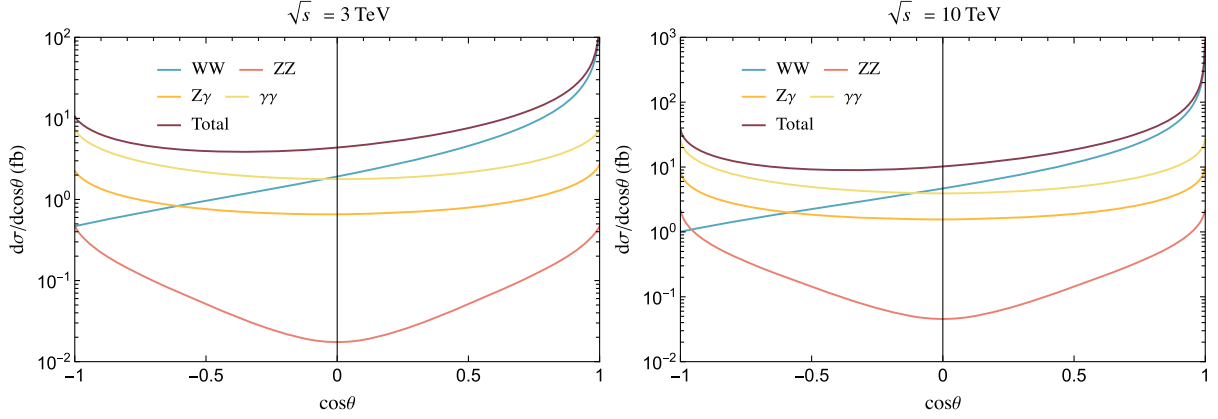
FIG. 4. The differential angular distribution for $\mu^+\mu^- \to t\bar{t} + X$ at muon colliders with $\sqrt{s} = 3$ TeV and $\sqrt{s} = 10$ TeV.

It turns out that the interference terms are small compared to the diagonal terms where $i_\pm = j_\pm$.

The angular distributions are shown in Fig. 4. The left panel is for the 3 TeV MuC, and the right one is for 10 TeV MuC. The dominant channel W^+W^- favors the forward direction due to the t-channel diagram exchanging intermediate b quark. For the neutral gauge bosons channels, they are symmetric with respect to $\theta = \pi/2$.

IV. PROJECTED SENSITIVITIES

After exploring both the rate and the kinematics, we perform signal analysis and derive the sensitivity of the Top Yukawa coupling deviations for 3 TeV and 10 TeV muon colliders. This section presents the projected sensitivities for the anomalous Top Yukawa coupling and VLQ model.

A. Top Yukawa precision

We show the relative change of the partonic cross section compared to the SM case due to the anomalous Top Yukawa coupling presented on the left panel of Fig. 5. Since the dominant signal comes from the WW channel

after convoluting with PDF, so we concentrate on this channel first to understand the leading contribution to the signal sensitivity. We can decompose the squared amplitude as

$$|\mathcal{M}_{\text{tot}}|^2 = |\mathcal{M}_{\text{SM}} + \delta_{yt}\mathcal{M}_{\text{sig}}|^2 = |\mathcal{M}_{\text{SM}}|^2 \\ + 2\delta_{yt}\text{Re}\mathcal{M}_{\text{SM}}^*\mathcal{M}_{\text{sig}} + \delta_{yt}^2|\mathcal{M}_{\text{sig}}|^2, \quad (24)$$

where δ_{yt} is the shift in Top Yukawa, and $\mathcal{M}_{\text{sig}}$ is the signal which comes from Higgs-mediated diagram.

The dashed lines in Fig. 5 show the signal-to-background ratio with linear in δ_{yt} contributions (as a typical choice for EFT analysis), and the solid lines include the terms proportional to δ_{yt}^2. Here, $\hat{\sigma}_{\text{SM}}$ is the sum of all SM cross sections with all helicities. A constructive interference between the SM background and the anomalous signal for $\delta_{yt} < 0$ exists, and similarly, a destructive interference for $\delta_{yt} > 0$ exists at linear order. As seen from the figure, if we only keep the linear term, while the modification to the s-channel Higgs amplitude scales as $\sqrt{\hat{s}}$ as shown in Eq. (3), $\Delta\hat{\sigma}/\hat{\sigma}_{\text{SM}}$ approaches a constant asymptotically.

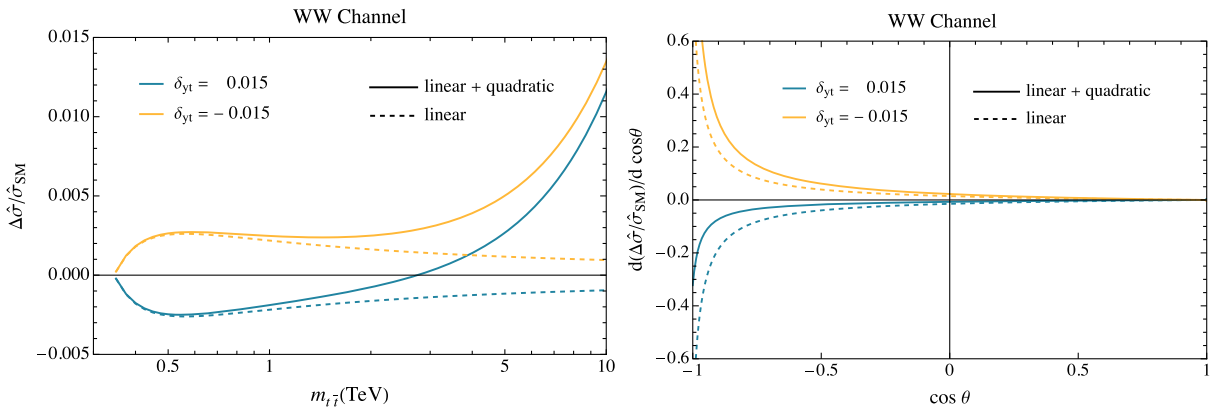

FIG. 5. The deviation of $WW \to t\bar{t}$ cross section from the Standard Model prediction value for benchmark choices of shift in Top Yukawa δ_{yt} as a function of (left panel) partonic center-of-mass energy and (right panel) scattering angle in the CM frame for a fixed partonic center-of-mass energy of 2 TeV. The solid and dashed lines are with and without the quadratic contributions, respectively.
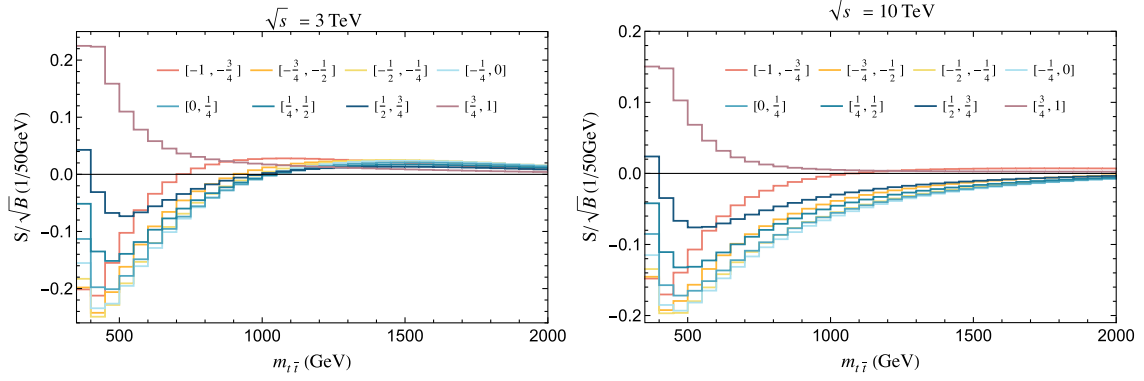
FIG. 6.   The significance of various bins in ranges of $m_{t\bar{t}}$ and $\cos\theta$ at 3 TeV and 10 TeV MuC. For illustration, we take δ_{yt} to be 0.015 for 10 TeV muon collider and 0.1 for 3 TeV muon collider, which are close to their one-sigma sensitivity. It can be seen from the figure that most of the sensitivity is coming from the interference term, near the threshold where the SM cross section peaks and the quadratic term contribution is negligible.

The ratio grows linearly with $\hat{s}$ in the high energy limit if we also include the quadratic term. As we show later, the sensitivity is dominated by the low invariant mass, linear regime. This implies the requirement for having systematic control at the subpercent level. As an electroweak machine, it should be achievable, and we also want to emphasize here the importance of precision calculation.

To understand the leading order behavior of these ratios, one should first remember that only the cross section with final top quark helicities $(\pm, \pm)$ receives contributions from δ_{yt} in the process $W_L^+ W_L^- \to t\bar{t}$. For the other two helicities, the Higgs exchange diagram is absent. More explicitly, we have

$$\frac{\Delta\hat{\sigma}}{\hat{\sigma}_{\rm SM}} \sim \frac{\sum_{\lambda=\pm} 2\delta_{yt}{\rm Re}\mathcal{M}_{\lambda\lambda}^h \mathcal{M}_{\lambda\lambda}^* + \delta_{yt}^2 |\mathcal{M}_{\lambda\lambda}^h|^2}{\sum |\mathcal{M}|^2}. \quad (25)$$

In the numerator, $\mathcal{M}_{\lambda\lambda}$ refers to all the SM amplitude with the top quark having the same helicities. $\mathcal{M}_{\lambda\lambda}^h$ denotes the amplitude for the Higgs-mediated diagram alone, which scales as $\sqrt{\hat{s}}$ in the high energy limit. From Table I, we can infer that the amplitude of $W_L^+ W_L^- \to t(\pm)\bar{t}(\pm)$ scales like $1/\sqrt{\hat{s}}$ in the high energy regime while the term proportional to δ_{yt} coming from the Higgs diagram scale as $\sqrt{\hat{s}}$. Thus, the interference between these two terms will have no scaling behavior. On the other hand, the sum of the squared amplitudes in SM approaches constant at the leading order. Therefore, the ratio of the linear term in δ_{yt} of $\Delta\hat{\sigma}$ and $\hat{\sigma}_{\rm SM}$ becomes asymptotically flat since both have a leading order constant term. The term quadratic in δ_{yt} scales as $\hat{s}$, and so the ratio including both terms increases linearly with $\hat{s}$ asymptotically.

The corresponding angular distribution of $\Delta\hat{\sigma}/\hat{\sigma}_{\rm SM}$ is shown on the right panel of Fig. 5 for the partonic $\sqrt{\hat{s}} = 2$ TeV. Note that $\mathcal{M}_{\rm sig}$ has no angular dependence due to the spin 0 Higgs boson exchange. Therefore, the angular dependence of the interference term is purely from the SM terms, and the term with quadratic δ_{yt} is flat. After dividing by the SM background contribution, the peak of the ratio occurs in the backward direction since the signal $\Delta\sigma$ is flatly distributed while the background favors the forward region.

To derive the sensitivity of the Top Yukawa coupling for the two muon collider benchmarks, we convolute the partonic signal cross sections with the PDF. For our analysis, we choose to bin the phase space in terms of the top quark pair invariant mass $m_{t\bar{t}}$ and the outgoing polar angle in the Center-Mass (CM) frame with respect to the μ^+ direction. Bin-by-bin signal significance after convolution is shown in Fig. 6, where the range of $\cos\theta$ is divided into eight equally sized bins, and $m_{t\bar{t}}$ is divided into 50 GeV bins to take into account finite resolution effects. From the figure, it is clear that our sensitivity will come from the linear term, which peaks near the threshold. More distribution can be found in Appendix B.

We perform a chi-square test to set bounds on anomalous Top Yukawa coupling. The results for the χ^2 analysis are presented in Fig. 7 for which we require the number of events in each bin to be at least 10. We compute the sensitivity $\Delta\chi_i^2 = S_i^2/B_i$ using the corresponding number of events for each bin. It is important to note that the signal (S_i) contains both the interference term and the quadratic term although the contribution of the quadratic term is negligible at the energy scale being considered. The total $\Delta\chi^2$ is obtained by summing over all the bins. This procedure is equivalent to a template double differential line-shape fit.

For a top quark pair, the branching ratios to various final states are 44% (hadronic), 44% (semileptonic), and 11% (fully leptonic) [43,44].[3] In our final state considerations, we conservatively take only the fully hadronic and

---

[3]Here, we split the τ final states into hadronic ones and leptonic ones with corresponding τ branch fractions.
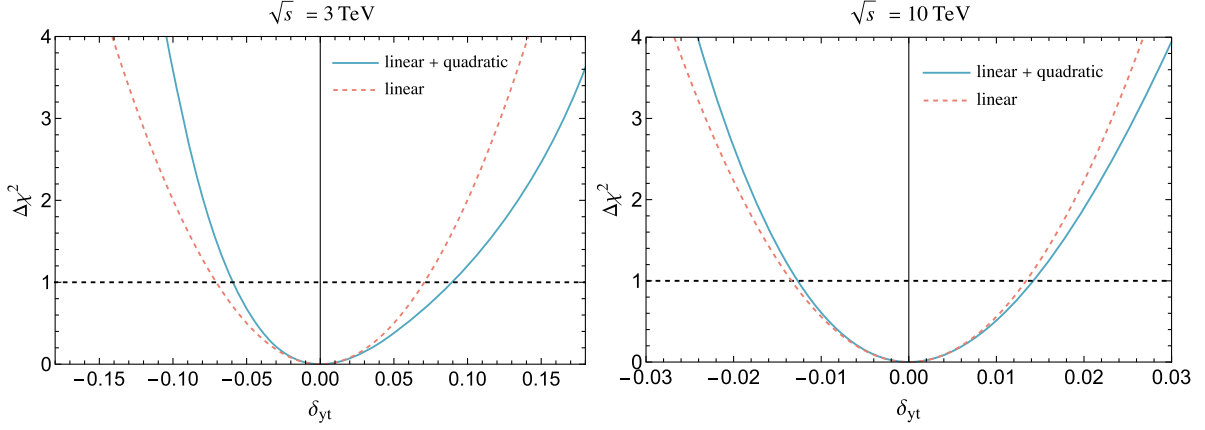
FIG. 7.   The $\Delta\chi^2$ as a function of δ_{yt} after summation over bins for $\sqrt{s} = 3$ TeV (left) and $\sqrt{s} = 10$ TeV (right). Contributions from linear terms (interference piece) and quadratic terms are included in the $\Delta\chi^2$ analysis for the solid curves, and dashed curves only include the linear terms. For the solid curves, the $\Delta\chi^2$ asymmetry results from including the quadratic term.

semileptonic $t\bar{t}$, as they are fully reconstructable without any sizable ambiguities. We also impose a cut on the outgoing t angle θ with respect to W^+ in the partonic center-of-mass frame,

$$10° < \theta < 170°, \tag{26}$$

to ensure high reconstruction efficiency and avoid the forward regions where shielding is needed due to beam-induced backgrounds. These cuts do not notably change our sensitivity since most of the signal significance comes from the central bins in angular distribution, as seen in Fig. 13.

The χ^2 analysis presented in Fig. 7 shows that the reach of δ_{yt} at one sigma Confidence Level (CL) is around $(-6\%, 9\%)$ for 3 TeV MuC and $(-1.3\%, 1.4\%)$ for 10 TeV MuC. The corresponding 2 sigma CL exclusions are around $(-11\%, 19\%)$ and $(-2.4\%, 3.1\%)$ for 3 and 10 TeV MuC, respectively.[4] It should be noted that in Fig. 7, we include the contributions from both the linear and quadratic terms of the signal. The resulting weight of these terms to the total $\Delta\chi^2$ is

$$\Delta\chi^2 = 2.0 \times 10^2 \delta_{yt}^2 - 1.2 \times 10^3 \delta_{yt}^3 + 3.9 \times 10^3 \delta_{yt}^4 \quad (3 \text{ TeV}), \tag{27}$$

$$\Delta\chi^2 = 5.6 \times 10^3 \delta_{yt}^2 - 4.8 \times 10^4 \delta_{yt}^3 + 2.6 \times 10^5 \delta_{yt}^4 \quad (10 \text{ TeV}). \tag{28}$$

As can be seen, the inclusion of the quadratic term results in producing asymmetric $\Delta\chi^2$ distribution. Furthermore, at one sigma C.L for both these colliders, if we neglect the quadratic term, δ_{yt} reach would be 7% for 3 TeV and 1.33% for 10 TeV case. Figure 7 also shows the results for only including the interference effects in dashed lines, which is conventionally done for EFT analysis. We can see the span of the sensitivity is very similar to the results, including the quadratic terms. One can obtain the corresponding $\Delta\chi^2$ expressions by dropping the last two terms in the above equations.

For more general Higgs precision fits, the relative contributions from the WW-fusion and ZZ-fusion channels need to be specified. Here, we also write down the $\Delta\chi^2$ in the widely used κ-framework [12,46–49]. Defining $\kappa_W = g_{WWh}/g_{WWh}^{\text{SM}}$, $\kappa_Z = g_{ZZh}/g_{ZZh}^{\text{SM}}$, $\kappa_t = y_t/y_t^{\text{SM}}$ in the kappa framework, we further perform the chi-square analysis for 3 TeV collider,

$$
\begin{aligned}
\Delta\chi^2 = {} & 2.2 \times 10^2 (\kappa_W \kappa_t - 1)^2 + 2.9 (\kappa_Z \kappa_t - 1)^2 - 23(\kappa_W \kappa_t - 1)(\kappa_Z \kappa_t - 1) \\
& - 1.2 \times 10^3 (\kappa_W \kappa_t - 1)^3 + 10(\kappa_Z \kappa_t - 1)^3 + 92(\kappa_W \kappa_t - 1)^2 (\kappa_Z \kappa_t - 1) \\
& - 1.3 \times 10^2 (\kappa_W \kappa_t - 1)(\kappa_Z \kappa_t - 1)^2 + 3.1 \times 10^3 (\kappa_W \kappa_t - 1)^4 + 38(\kappa_Z \kappa_t - 1)^4 \\
& + 6.9 \times 10^2 (\kappa_W \kappa_t - 1)^2 (\kappa_Z \kappa_t - 1)^2,
\end{aligned}
\tag{29}
$$

---

[4]If one uses only the semileptonic $t\bar{t}$, the 95% CL limit on the anomalous top coupling is projected to be 5.6%. This is highly consistent with the simulation-based study [45] at a 10 TeV MuC.

and for 10 TeV,

$$
\begin{aligned}
\Delta\chi^2 = {} & 6.2 \times 10^3 (\kappa_W \kappa_t - 1)^2 + 1 \times 10^2 (\kappa_Z \kappa_t - 1)^2 - 6.6 \times 10^2 (\kappa_W \kappa_t - 1)(\kappa_Z \kappa_t - 1) \\
& - 4.7 \times 10^4 (\kappa_W \kappa_t - 1)^3 + 4.4 \times 10^2 (\kappa_Z \kappa_t - 1)^3 + 4.0 \times 10^3 (\kappa_W \kappa_t - 1)^2 (\kappa_Z \kappa_t - 1) \\
& - 5.1 \times 10^3 (\kappa_W \kappa_t - 1)(\kappa_Z \kappa_t - 1)^2 + 2.1 \times 10^5 (\kappa_W \kappa_t - 1)^4 + 2.6 \times 10^3 (\kappa_Z \kappa_t - 1)^4 \\
& + 4.7 \times 10^4 (\kappa_W \kappa_t - 1)^2 (\kappa_Z \kappa_t - 1)^2.
\end{aligned}
\tag{30}
$$

Similarly, one can obtain the interference alone contribution by dropping all terms other than the first lines of the above equations. These equations also reveal that the sensitivity reach is dominated by the WW channel. Note that here, we assume no forward muon tagging, which means the ZZ fusion and WW fusion are indistinguishable at the analysis level. In other words, they share the same backgrounds. If one can tag the forward muons and hence reduce the ZZ-fusion backgrounds, the relative importance and contribution will change.
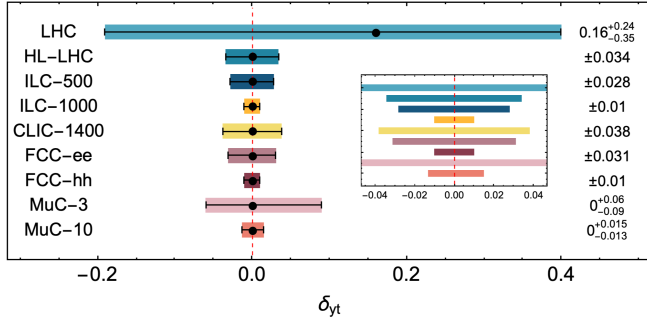

FIG. 8.   The reach plot for δ_{yt} at 1σ sensitivity on various colliders with their best projections through various processes. The bound on the Top Yukawa shift factor δ_{yt} from (top to bottom) the current LHC [15,50], future High-Luminosity LHC [51], proposed ILC [52,53], CLIC [54], FCC-ee, and FCC-hh [55]. In the subpanel, we show the zoom-in version to compare different bars in the smaller range.
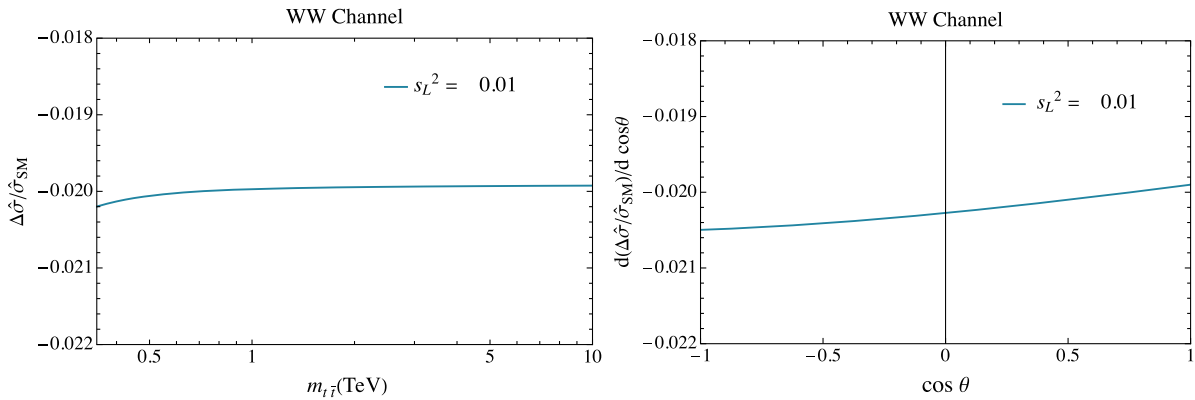
The δ_{yt} reach at one sigma CL is $(-6\%, 8\%)$ for 3 TeV MuC and $(-1.2\%, 1.4\%)$ for 10 TeV MuC. In Fig. 8, we show the one sigma sensitivity on δ_{yt} at the current LHC, HL-LHC, ILC-500, ILC-100, CLIC, FCC-ee, and FCC-hh and compare them with our results at muon colliders of 3 and 10 TeV. At present, the LHC experimental constraint is at the $O(10\%)$ level. The future 100 TeV FCC-hh can probe the Top Yukawa coupling to around 1%. We show here the muon collider can achieve comparable sensitivity.

B. VLQ model

Now we study this channel in the VLQ model, where the Top Yukawa modification correlates with other coupling modifications. Analogous to our previous discussion, we first focus on the deviation in the partonic cross section of the $W^+ W^- \to t\bar{t}$ channel which is shown in Fig. 9 for $s_L^2 = 0.01$. Since this is a UV-complete model, we keep all the higher order terms of δ_{yt} or s_L^2. We observe that the relative change decreases when the center-of-mass energy increases from the threshold energy and becomes almost flat as $\sqrt{\hat{s}}$ exceeds around 1 TeV. To understand this result, first, we note that the dominant (helicity) amplitude for the SM background is asymptotically flat. Since we are working in the weakly coupled UV-completed model, the amplitude should also be unitarized. This explains why the two distributions are relatively flat. It is interesting to note that the angular distribution of the BSM-to-SM ratio $\Delta\hat{\sigma}/\hat{\sigma}_{\mathrm{SM}}$ is also nearly flat, which suggests that the signal

FIG. 9.   The relative shift of the partonic cross section for the WW channel in VLQ model as a function of $\sqrt{\hat{s}}$ and the polar angle $\cos\theta$.
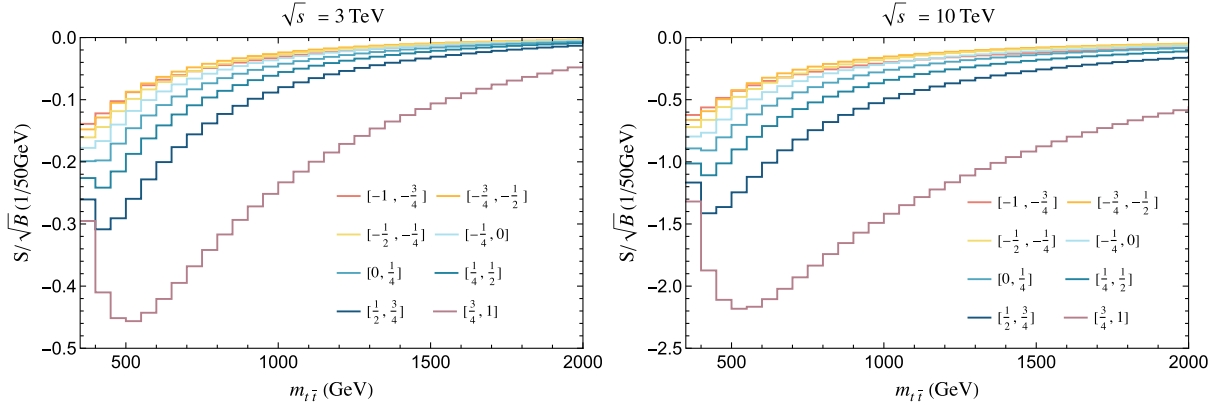
FIG. 10. $S/\sqrt{B}$ for $s_L^2 = 0.01$ for both a 3 TeV (left) and a 10 TeV (right) MuC. We cut the whole space in terms of the invariant mass $m_{t\bar{t}}$ and the angular variable $\cos\theta$. Different colors denote the bin range of $\cos\theta$.

follows the shape of the background. In other words, the VLQ signal shifts the SM cross section.

The shifting can be explained by noting that the leading order contribution for $W_L^+ W_L^- \to t\bar{t}$ is dominated by the left-handed current as we have emphasized in Sec. III A. For our VLQ analysis, the t_L field is rescaled by c_L. Hence, the amplitudes of the two channels are shifted by a common factor of $-s_L^2$. This explains why the relative shifting factor for the cross section is approaching $-2s_L^2$ in the high energy regime and is almost independent of the theta angle.

On the other hand, we can also compute using the Goldstone boson equivalence theorem. As discussed in Sec. II, if there is only a single operator EFT $\mathcal{O}_y^t$, a new contact vertex $\phi^+\phi^- t\bar{t}$ is generated, leading to the energy growing behavior. While in the VLQ case, two other operators can generate the new coupling $i(\partial_\mu\phi^+\bar{t}_L\gamma^\mu b_L - \partial_\mu\phi^-\bar{b}_L\gamma^\mu t_L)$ that modifies the t-channel diagram amplitude which also has the energy growing behavior. The correlated Wilson coefficients guarantee the cancellation of individual unitarity violations.

In Fig. 10, we show the $S/\sqrt{B}$ distribution over the top quark pair invariant mass $m_{t\bar{t}}$ after dividing the phase space into various bins. Curves with different colors refer to the angular bins. The peak values for the significance occur at low $m_{t\bar{t}}$ regime as well as the forward region. As S/B is almost a constant, we get stronger sensitivity in the forward direction and a low $m_{t\bar{t}}$ region where the statistics are large.

We follow the same procedure described in the previous section to estimate the projected sensitivity and show the results in Fig. 11. The anomalous Top Yukawa coupling shift can be tested to around 0.5% at 3 TeV MuC and 0.1% at 10 TeV MuC at one sigma level. In Fig. 12, we show various 95% exclusion regions on the $m_T - \delta_{yt}$ plane. The blue, orange, and pink dashed lines refer to the bound from the Higgs decaying to di-gluon precision measurement at 10 TeV MuC and the $t\bar{t}$ channel at 3 TeV MuC and 10 TeV MuC, respectively. The coupling is strong in the light-yellow region, violating perturbative unitarity in the Higgs-mediated four-fermi scattering process, with the UV Yuakawa coupling $\lambda_0 > O(10)$ in Eq. (13). The shaded
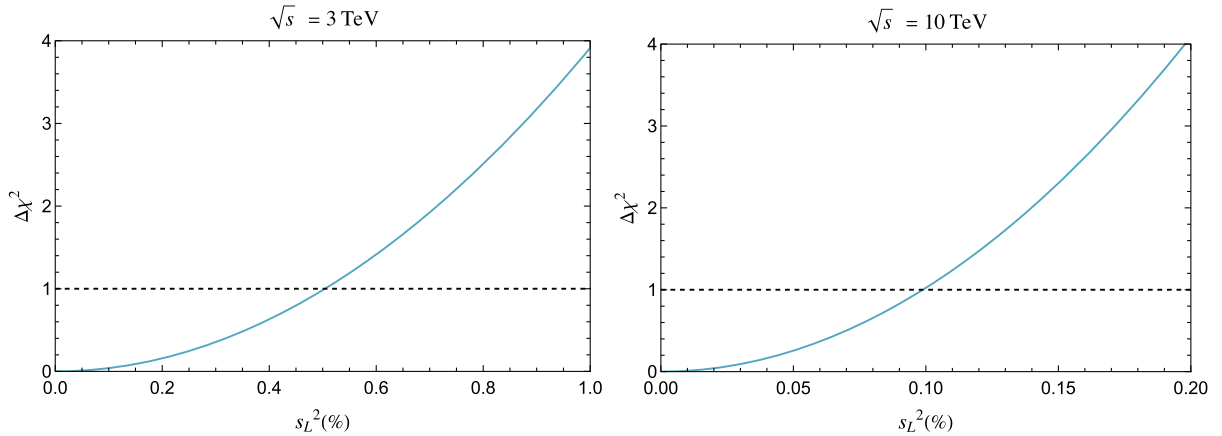

FIG. 11. The $\Delta\chi^2$ as a function of $s_L^2 = -\delta_{yt}$ after summation over bins for $\sqrt{s} = 3$ TeV (left) and $\sqrt{s} = 10$ TeV (right) in VLQ model.
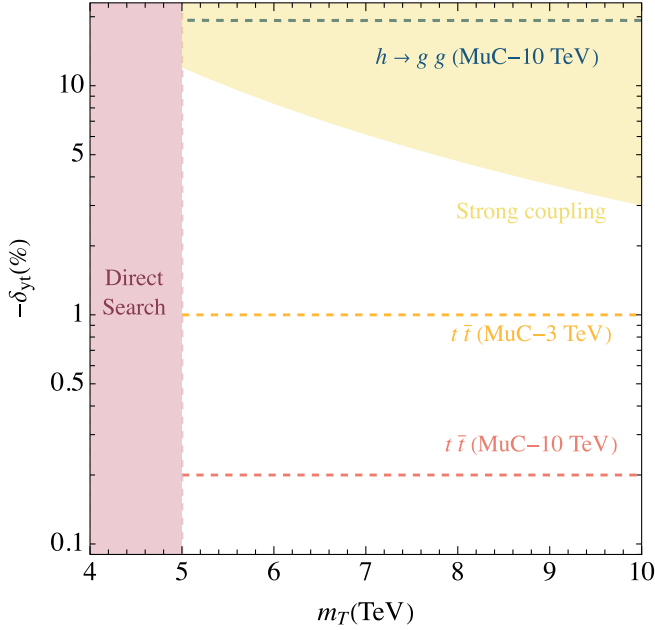
FIG. 12. The 95% CL exclusion sensitivity for the parameters in VLQ model. The blue dashed line is from the top quark pair production and the Higgs decaying to di-gluon measurement [13]. The orange and pink dashed lines refer to the exclusion sensitivity at 95% exclusion limit. The light-yellow region denotes the strong coupling regime where the UV Yukawa coupling λ_0 is larger than $O(10)$. We expect the region for $m_T < 5$ TeV can be covered by the direct search, as the $T\bar{T}$ pair production is kinematically allowed. More computation details for the VLQ model can be found in Appendix C.

region for $m_T < 5$ TeV is denoted as "Direct Search," where the $T\bar{T}$ production is kinematically allowed. We also made an estimate of the reach of the single heavy VLQ search at the 10 TeV MuC, and this channel can exclude δ_{yt} to be around the one percent level. However, given the sensitivity dependence on the detailed realization of VLQ, e.g., the existence of heavy bottoms, we do not show the estimation here. For a similar reason, we also do not show electroweak precision from future Z-pole programs in this plot.

V. CONCLUSION

In this work, we have examined the prospects for measuring the Top Yukawa coupling at upcoming high energy muon colliders, focusing on two benchmark center-of-mass energies: 3 TeV and 10 TeV. We thoroughly investigated the partonic cross sections of the processes $VV \to t\bar{t}$ for various helicities and delved into the differential kinematical distributions. Upon convolution with the electroweak gauge boson PDFs, it becomes evident that the dominant partonic channel is the scattering of longitudinal W bosons into a right-handed top quark and a left-handed anti-top-quark.

We utilized two scenarios to characterize deviations from the Standard Model (SM) Top Yukawa coupling. We first

considered the case in which a single dimension-six EFT operator can encapsulate the influences of new physics, denoted as $\mathcal{O}_y^t$. Here, the primary effect is an anomalous deviation in the Top Yukawa coupling. Consequently, the amplitude of $W^+W^- \to t\bar{t}$ rises with the partonic center-of-mass energy, leading to significant discrepancies from SM predictions at larger $m_{t\bar{t}}$. In our second approach, taking inspiration from a UV-completed model, we introduced a pair of singlet vectorlike quarks. Post electroweak symmetry breaking, a mixture occurs between the top quark and the heavy VLQ, altering the Top Yukawa coupling. In this scenario, the amplitude or cross section's relative shift remains mostly flat across a broad range of $m_{t\bar{t}}$.

Constraints on the Top Yukawa deviation can be established, assuming future measurements agree with SM. Segmenting the entire phase space according to the production polar angle and the invariant mass of the top quark pair allows for chi-square analysis. For the EFT model, the Top Yukawa measurement precision approaches the percent level, providing valuable measurements of Top Yukawa beyond HL-LHC. The results are summarized in Fig. 8. Furthermore, we provide chi-square data for global fit to the Higgs signal in Eqs. (27)–(30). Importantly, compared to the conventional channel of $t\bar{t}h$ [13,14], our method is more than one order of magnitude better in projected precision and also sensitive to the sign of the Top Yukawa deviation. Conversely, in the VLQ model, this precision is further improved to nearing the per mil level. These high precision measurements also require precision calculation from the theory side to ensure their robustness. We estimated the leading order perturbative correction would be at the percent level.

The data associated with the figures in this paper can be accessed via GitHub [56].

APPENDIX A: HELICITY AMPLITUDE

In this section, we focus on the amplitude of $W^+W^- \to t\bar{t}$ and its analytic expressions. The total amplitude for a given helicity configuration can be written as the sum of contributions from four channels,

$$\mathcal{M}_{h_{w^+}h_{w^-},h_th_{\bar{t}}} = \mathcal{M}^\gamma + \mathcal{M}^Z + \mathcal{M}^b + \mathcal{M}^h, \quad \text{(A1)}$$

where the h in the subscript refers to the corresponding helicities. $\mathcal{M}^{\gamma/Z/h}$ refers to the s-channel contribution, and $\mathcal{M}^b$ refers to the t-channel diagram. We compute the amplitude in the massless b-quark limit. Also, we choose the incoming W^+ to be aligned along the z axis and define the scattering angle θ as the polar angle between W^+ and the t quark in the partonic center-of-mass frame. Thus, with this definition, we have in the massless b quark limit,

$$s = 4E_t^2 = 4E_W^2, \quad t = -\frac{s}{4}(\beta_t^2 + \beta_W^2 - 2\beta_t\beta_W\cos\theta). \quad \text{(A2)}$$

Here, $E_{t,W}$ is the center-of-mass energy of each particle, and $\beta_{t,W}^2 = 1 - 4m_{t,W}^2/s$. In this section, all the variables are partonic variables, and we drop the hat for abbreviation as there is no ambiguity. For our calculations, we use the explicit form of four spinors and polarization vectors in the center-of-mass frame and calculate the helicity amplitudes. Wigner d functions are explicitly given by

$$d_{0,0}^2 = \frac{1}{2}(3\cos^2\theta - 1), \quad d_{2,0}^2 = \sqrt{\frac{3}{8}}\sin^2\theta, \quad \text{(A3)}$$

$$d_{1,0}^2 = -d_{-1,0}^2 = -\sqrt{\frac{3}{8}}\sin 2\theta, \quad \text{(A4)}$$

$$d_{2,1}^2 = -d_{-2,-1}^2 = -\frac{1}{2}(1 + \cos\theta)\sin\theta, \quad \text{(A5)}$$

$$d_{2,-1}^2 = -d_{-2,1}^2 = -\frac{1}{2}(1 - \cos\theta)\sin\theta, \quad \text{(A6)}$$

$$d_{1,1}^2 = d_{-1,-1}^2 = \frac{1}{2}(2\cos^2\theta + \cos\theta - 1), \quad \text{(A7)}$$

$$d_{1,-1}^2 = d_{-1,1}^2 = \frac{1}{2}(-2\cos^2\theta + \cos\theta + 1), \quad \text{(A8)}$$

$$d_{1,1}^1 = d_{-1,-1}^1 = \frac{1}{2}(1 + \cos\theta), \quad \text{(A9)}$$

$$d_{1,-1}^1 = d_{-1,1}^1 = \frac{1}{2}(1 - \cos\theta), \quad \text{(A10)}$$

$$d_{1,0}^1 = -d_{-1,0}^1 = -\sqrt{\frac{1}{2}}\sin\theta, \quad \text{(A11)}$$

$$d_{0,0}^1 = \cos\theta, \quad d_{0,0}^0 = 1, \quad \text{(A12)}$$

$$d_{m,m'}^j = (-1)^{m-m'}d_{m',m}^j = d_{-m',-m}^j. \quad \text{(A13)}$$

(i) $(00, ++)$

$$\mathcal{M}_{00,++}^\gamma = \frac{2}{3}[2\sqrt{2}G_F m_t s_w^2 s^{1/2}\beta_W(3 - \beta_W^2)]d_{0,0}^1, \quad \text{(A14)}$$

$$\mathcal{M}_{00,++}^Z = \frac{2}{3}\left[\frac{1}{\sqrt{2}}G_F m_t\left(\frac{3}{2} - 4s_w^2\right)\frac{s^{3/2}}{s - M_Z^2}\beta_W(3 - \beta_W^2)\right]d_{0,0}^1, \quad \text{(A15)}$$

$$\mathcal{M}_{00,++}^b = \frac{1}{2\sqrt{2}}G_F m_t\frac{s^{3/2}}{t}\left[\beta_t\left(\frac{1}{3} + \beta_W^2\right) + \beta_W(1 - \beta_W^2)d_{0,0}^1 - \frac{4}{3}\beta_t d_{0,0}^2\right], \quad \text{(A16)}$$

$$\mathcal{M}_{00,++}^h = \frac{1}{2}G_F y_t v\frac{s^{3/2}}{s - m_H^2}\beta_t(1 + \beta_W^2). \quad \text{(A17)}$$

(ii) $(00, +-)$

$$\mathcal{M}_{00,+-}^\gamma = -\frac{2}{3}[2G_F s_w^2 s\beta_W(3 - \beta_W^2)]d_{0,1}^1, \quad \text{(A18)}$$

$$\mathcal{M}_{00,+-}^Z = -\frac{2}{3}\left[\frac{1}{2}G_F\left(\frac{3}{2}(1 - \beta_t) - 4s_w^2\right)\frac{s^2}{s - M_Z^2}\beta_W(3 - \beta_W^2)\right]d_{0,1}^1, \quad \text{(A19)}$$

$$\mathcal{M}_{00,+-}^b = \frac{1}{2}G_F\frac{s^2}{t}(1 - \beta_t)\left[\left(\beta_W\beta_t - \frac{1}{2}\beta_W(1 - \beta_W^2)\right)d_{0,1}^1 + \sqrt{\frac{2}{3}}\beta_t d_{0,1}^2\right], \quad \text{(A20)}$$

$$\mathcal{M}^h_{00,+-} = 0. \tag{A21}$$

(iii) $(00, -+)$

$$\mathcal{M}^\gamma_{00,-+} = \frac{2}{3}[2G_F s_w^2 s \beta_W (3 - \beta_W^2)]d^1_{0,-1}, \tag{A22}$$

$$\mathcal{M}^Z_{00,-+} = \frac{2}{3}\left[\frac{1}{2}G_F\left(\frac{3}{2}(1+\beta_t) - 4s_w^2\right)\frac{s^2}{s - M_Z^2}\beta_W(3 - \beta_W^2)\right]d^1_{0,-1}, \tag{A23}$$

$$\mathcal{M}^b_{00,-+} = -\frac{1}{2}G_F\frac{s^2}{t}(1+\beta_t)\left[\left(-\beta_W\beta_t - \frac{1}{2}\beta_W(1-\beta_W^2)\right)d^1_{0,-1} + \sqrt{\frac{2}{3}}\beta_t d^2_{0,-1}\right], \tag{A24}$$

$$\mathcal{M}^h_{00,-+} = 0. \tag{A25}$$

(iv) $(00, --)$

$$\mathcal{M}^\gamma_{00,--} = -\frac{2}{3}[2\sqrt{2}G_F m_t s_w^2 s^{1/2}\beta_W(3 - \beta_W^2)]d^1_{0,0}, \tag{A26}$$

$$\mathcal{M}^Z_{00,--} = -\frac{2}{3}\left[\frac{1}{\sqrt{2}}G_F m_t\left(\frac{3}{2} - 4s_w^2\right)\frac{s^{3/2}}{s - M_Z^2}\beta_W(3 - \beta_W^2)\right]d^1_{0,0}, \tag{A27}$$

$$\mathcal{M}^b_{00,--} = -\frac{1}{2\sqrt{2}}G_F m_t \frac{s^{3/2}}{t}\left[\beta_t\left(\frac{1}{3} + \beta_W^2\right) + \beta_W(1 - \beta_W^2)d^1_{0,0} - \frac{4}{3}\beta_t d^2_{0,0}\right], \tag{A28}$$

$$\mathcal{M}^h_{00,--} = -\frac{1}{2}G_F y_t v \frac{s^{3/2}}{s - m_H^2}\beta_t(1 + \beta_W^2). \tag{A29}$$

(i) $(-0, ++)$

$$\mathcal{M}^\gamma_{-0,++} = \frac{2}{3}[8\sqrt{2}G_F m_t m_W s_w^2 \beta_W]d^1_{-1,0}, \tag{A30}$$

$$\mathcal{M}^Z_{-0,++} = \frac{2}{3}\left[2\sqrt{2}G_F m_t m_W\left(\frac{3}{2} - 4s_w^2\right)\frac{s}{s - M_Z^2}\beta_W\right]d^1_{-1,0}, \tag{A31}$$

$$\mathcal{M}^b_{-0,++} = -\frac{1}{\sqrt{2}}G_F m_t m_W \frac{s}{t}\left[(-\beta_t\beta_W - \beta_t - \beta_W(1-\beta_W))d^1_{-1,0} + \frac{2}{\sqrt{3}}\beta_t d^2_{-1,0}\right], \tag{A32}$$

$$\mathcal{M}^h_{-0,++} = 0. \tag{A33}$$

(ii) $(-0, +-)$

$$\mathcal{M}^\gamma_{-0,+-} = -\frac{2}{3}[8G_F m_W s_w^2 s^{1/2}\beta_W]d^1_{-1,1}, \tag{A34}$$

$$\mathcal{M}^Z_{-0,+-} = -\frac{2}{3}\left[2G_F m_W\left(\frac{3}{2}(1-\beta_t) - 4s_w^2\right)\frac{s^{3/2}}{s - M_Z^2}\beta_W\right]d^1_{-1,1}, \tag{A35}$$

$$\mathcal{M}^b_{-0,+-} = \frac{1}{2}G_F m_W \frac{s^{3/2}}{t}(1-\beta_t)[(-\beta_W(1-\beta_W) + \beta_t\beta_W)d^1_{-1,1} + \beta_t d^2_{-1,1}], \tag{A36}$$

$$\mathcal{M}^h_{-0,+-} = 0. \tag{A37}$$

(iii) $(-0, -+)$

$$\mathcal{M}^\gamma_{-0,-+} = \frac{2}{3}[8G_F s_w^2 m_W s^{1/2} \beta_W] d^1_{-1,-1}, \tag{A38}$$

$$\mathcal{M}^Z_{-0,-+} = \frac{2}{3}\left[2G_F m_W \left(\frac{3}{2}(1+\beta_t) - 4s_w^2\right) \frac{s^{3/2}}{s - M_Z^2} \beta_W\right] d^1_{-1,-1}, \tag{A39}$$

$$\mathcal{M}^b_{-0,-+} = -\frac{1}{2} G_F m_W \frac{s^{3/2}}{t}(1+\beta_t)[(-\beta_W(1-\beta_W) - \beta_t\beta_W)d^1_{-1,-1} + \beta_t d^2_{-1,-1}], \tag{A40}$$

$$\mathcal{M}^h_{-0,-+} = 0. \tag{A41}$$

(iv) $(-0, --)$

$$\mathcal{M}^\gamma_{-0,--} = -\frac{2}{3}[8\sqrt{2}G_F m_t m_W s_w^2 \beta_W] d^1_{-1,0}, \tag{A42}$$

$$\mathcal{M}^Z_{-0,--} = -\frac{2}{3}\left[2\sqrt{2}G_F m_t m_W \left(\frac{3}{2} - 4s_w^2\right) \frac{s}{s - M_Z^2} \beta_W\right] d^1_{-1,0}, \tag{A43}$$

$$\mathcal{M}^b_{-0,--} = \frac{1}{\sqrt{2}} G_F m_t m_W \frac{s}{t}\left[(\beta_t\beta_W + \beta_t - \beta_W(1-\beta_W))d^1_{-1,0} + \frac{2}{\sqrt{3}}\beta_t d^2_{-1,0}\right], \tag{A44}$$

$$\mathcal{M}^h_{-0,--} = 0. \tag{A45}$$

The corresponding amplitude for $h_{W^+} = 0$, $h_{W^-} = +$ can be found be by *CP* transforming the above expressions.

(i) $(+0, ++)$

$$\mathcal{M}^\gamma_{+0,++} = \frac{2}{3}(8\sqrt{2}G_F m_t m_W s_w^2 \beta_W) d^1_{1,0}, \tag{A46}$$

$$\mathcal{M}^Z_{+0,++} = \frac{2}{3}\left[2\sqrt{2}G_F m_t m_W \left(\frac{3}{2} - 4s_w^2\right) \frac{s}{s - M_Z^2} \beta_W\right] d^1_{1,0}, \tag{A47}$$

$$\mathcal{M}^b_{+0,++} = \frac{1}{\sqrt{2}} G_F m_t m_W \frac{s}{t}\left[(\beta_t\beta_W - \beta_t + \beta_W(1+\beta_W))d^1_{1,0} - \frac{2}{\sqrt{3}}\beta_t d^2_{1,0}\right], \tag{A48}$$

$$\mathcal{M}^h_{+0,++} = 0. \tag{A49}$$

(ii) $(+0, +-)$

$$\mathcal{M}^\gamma_{+0,+-} = -\frac{2}{3}[8G_F s_w^2 m_W s^{1/2} \beta_W] d^1_{1,1}, \tag{A50}$$

$$\mathcal{M}^Z_{+0,+-} = -\frac{2}{3}\left[2G_F m_W \left(\frac{3}{2}(1-\beta_t) - 4s_w^2\right) \frac{s^{3/2}}{s - M_Z^2} \beta_W\right] d^1_{1,1}, \tag{A51}$$

$$\mathcal{M}^b_{+0,+-} = -\frac{1}{2} G_F m_W \frac{s^{3/2}}{t}(1-\beta_t)[(\beta_W(1+\beta_W) - \beta_t\beta_W)d^1_{1,1} - \beta_t d^2_{1,1}], \tag{A52}$$

$$\mathcal{M}^h_{+0,+-} = 0. \tag{A53}$$

(iii) $(+0, -+)$

$$\mathcal{M}^{\gamma}_{+0,-+} = \frac{2}{3}[8 G_F s_w^2 m_W s^{1/2} \beta_W] d^1_{1,-1}, \tag{A54}$$

$$\mathcal{M}^{Z}_{+0,-+} = \frac{2}{3}\left[2 G_F m_W \left(\frac{3}{2}(1 + \beta_t) - 4 s_w^2\right) \frac{s^{3/2}}{s - M_Z^2}\beta_W\right] d^1_{1,-1}, \tag{A55}$$

$$\mathcal{M}^{b}_{+0,-+} = \frac{1}{2} G_F m_W \frac{s^{3/2}}{t}(1 + \beta_t)[(\beta_W(1 + \beta_W) + \beta_t\beta_W)d^1_{1,-1} - \beta_t d^2_{1,-1}], \tag{A56}$$

$$\mathcal{M}^{h}_{+0,-+} = 0. \tag{A57}$$

(iv) $(+0, --)$

$$\mathcal{M}^{\gamma}_{+0,--} = -\frac{2}{3}[8\sqrt{2} G_F m_t m_W s_w^2 \beta_W] d^1_{1,0}, \tag{A58}$$

$$\mathcal{M}^{Z}_{+0,--} = -\frac{2}{3}\left[2\sqrt{2} G_F m_t m_W \frac{s}{s - M_Z^2}\left(\frac{3}{2} - 4 s_w^2\right)\beta_W\right] d^1_{1,0}, \tag{A59}$$

$$\mathcal{M}^{b}_{+0,--} = -\frac{1}{\sqrt{2}} G_F m_t m_W \frac{s}{t}\left[(-\beta_t\beta_W + \beta_t + \beta_W(1 + \beta_W))d^1_{1,0} - \frac{2}{\sqrt{3}}\beta_t d^2_{1,0}\right], \tag{A60}$$

$$\mathcal{M}^{h}_{+0,--} = 0. \tag{A61}$$

Amplitudes for $h_{W^+} = 0$, $h_{W^-} = -$ are related by *CP* transformation.

(i) $(++, ++)$

$$\mathcal{M}^{\gamma}_{++,++} = -\frac{2}{3}[8\sqrt{2} G_F m_t m_W^2 s_w^2 s^{-1/2} \beta_W] d^1_{0,0}, \tag{A62}$$

$$\mathcal{M}^{Z}_{++,++} = -\frac{2}{3}\left[2\sqrt{2} G_F m_t m_W^2 \left(\frac{3}{2} - 4 s_w^2\right) \frac{s^{1/2}}{s - M_Z^2}\beta_W\right] d^1_{0,0}, \tag{A63}$$

$$\mathcal{M}^{b}_{++,++} = 2\sqrt{2} G_F m_t m_W^2 \frac{s^{1/2}}{t}\left[\frac{1}{6}(\beta_t - 3\beta_W) + \frac{d^1_{0,0}}{2}(\beta_t - \beta_W) + \frac{d^2_{0,0}}{3}\beta_t\right], \tag{A64}$$

$$\mathcal{M}^{h}_{++,++} = 2 G_F \beta_t y_t v m_W^2 \frac{\sqrt{s}}{s - m_H^2}. \tag{A65}$$

(ii) $(++, +-)$

$$\mathcal{M}^{\gamma}_{++,+-} = \frac{2}{3}[8 G_F m_W^2 s_w^2 \beta_W] d^1_{0,1}, \tag{A66}$$

$$\mathcal{M}^{Z}_{++,+-} = \frac{2}{3}\left[2 G_F m_W^2 \left(\frac{3}{2}(1 - \beta_t) - 4 s_w^2\right) \frac{s}{s - M_Z^2}\beta_W\right] d^1_{0,1}, \tag{A67}$$

$$\mathcal{M}^{b}_{++,+-} = G_F m_W^2 \frac{s}{t}(1 - \beta_t)\left[\beta_W d^1_{0,1} - \sqrt{\frac{1}{3}}\beta_t d^2_{0,1}\right], \tag{A68}$$

$$\mathcal{M}^{h}_{++,+-} = 0. \tag{A69}$$

(iii) $(++,-+)$

$$\mathcal{M}^{\gamma}_{++,-+} = -\frac{2}{3}[8G_F m_W^2 s_w^2 \beta_W] d^1_{0,-1}, \quad \text{(A70)}$$

$$\mathcal{M}^Z_{++,-+} = -\frac{2}{3}\left[2G_F m_W^2\left(\frac{3}{2}(1+\beta_t)-4s_w^2\right)\right.$$
$$\left. \times \frac{s}{s-M_Z^2}\beta_W\right]d^1_{0,-1}, \quad \text{(A71)}$$

$$\mathcal{M}^b_{++,-+} = -G_F m_W^2 \frac{s}{t}(1+\beta_t)\left[\beta_W d^1_{0,1} - \sqrt{\frac{1}{3}}\beta_t d^2_{0,1}\right], \quad \text{(A72)}$$

$$\mathcal{M}^h_{++,-+} = 0. \quad \text{(A73)}$$

(iv) $(++,--)$

$$\mathcal{M}^{\gamma}_{++,--} = \frac{2}{3}[8\sqrt{2}G_F m_t m_W^2 s_w^2 s^{-1/2}\beta_W] d^1_{0,0}, \quad \text{(A74)}$$

$$\mathcal{M}^Z_{++,--} = \frac{2}{3}\left[2\sqrt{2}G_F m_t m_W^2\left(\frac{3}{2}-4s_w^2\right)\right.$$
$$\left. \times \frac{s^{1/2}}{s-M_Z^2}\beta_W\right]d^1_{0,0}, \quad \text{(A75)}$$

$$\mathcal{M}^b_{++,--} = -2\sqrt{2}G_F m_t m_W^2 \frac{s^{1/2}}{t}$$
$$\times \left[\frac{1}{6}(\beta_t+3\beta_W)-\frac{d^1_{0,0}}{2}(\beta_t+\beta_W)+\frac{d^2_{0,0}}{3}\beta_t\right], \quad \text{(A76)}$$

$$\mathcal{M}^h_{++,--} = -2G_F \beta_t y_t v m_W^2 \frac{\sqrt{s}}{s-m_H^2}. \quad \text{(A77)}$$

Amplitudes for $h_{W^+}=-$, $h_{W^-}=-$ are related by CP transformation.

(i) $(+-,++)$

$$\mathcal{M}^{\gamma}_{+-,++} = 0, \quad \text{(A78)}$$

$$\mathcal{M}^Z_{+-,++} = 0, \quad \text{(A79)}$$

$$\mathcal{M}^b_{+-,++} = \frac{4}{\sqrt{3}}G_F m_t m_W^2 \frac{s^{1/2}}{t}\beta_t d^2_{2,0}, \quad \text{(A80)}$$

$$\mathcal{M}^h_{+-,++} = 0. \quad \text{(A81)}$$

(ii) $(+-,+-)$

$$\mathcal{M}^{\gamma}_{+-,+-} = 0, \quad \text{(A82)}$$

$$\mathcal{M}^Z_{+-,+-} = 0, \quad \text{(A83)}$$

$$\mathcal{M}^b_{+-,+-} = -\sqrt{2}G_F m_W^2 \frac{s}{t}\beta_t(1-\beta_t)d^2_{2,1}, \quad \text{(A84)}$$

$$\mathcal{M}^h_{+-,+-} = 0. \quad \text{(A85)}$$

(iii) $(+-,-+)$

$$\mathcal{M}^{\gamma}_{+-,-+} = 0, \quad \text{(A86)}$$

$$\mathcal{M}^Z_{+-,-+} = 0, \quad \text{(A87)}$$

$$\mathcal{M}^b_{+-,-+} = \sqrt{2}G_F m_W^2 \frac{s}{t}\beta_t(1+\beta_t)d^2_{2,-1}, \quad \text{(A88)}$$

$$\mathcal{M}^h_{+-,-+} = 0. \quad \text{(A89)}$$

(iv) $(+-,--)$

$$\mathcal{M}^{\gamma}_{+-,--} = 0, \quad \text{(A90)}$$

$$\mathcal{M}^Z_{+-,--} = 0, \quad \text{(A91)}$$

$$\mathcal{M}^b_{+-,--} = -\frac{4}{\sqrt{3}}G_F m_t m_W^2 \frac{s^{1/2}}{t}\beta_t d^2_{2,0}, \quad \text{(A92)}$$

$$\mathcal{M}^h_{+-,--} = 0. \quad \text{(A93)}$$

Amplitudes for $h_{W^+}=-$, $h_{W^-}=+$ are related by CP transformation.

APPENDIX B: SIGNAL VS BACKGROUND

In this section, we show the dependence of the significance on the angular variable $\cos\theta$ and the top quark invariant mass $m_{t\bar{t}}$ in the center-of-mass frame for both the 3 TeV and 10 TeV colliders, respectively. Polar angle θ is defined in the partonic frame and is the angle between the t quark and W^+ boson.

We show angular dependence of signal significance for a $\sqrt{s} = 10$ TeV and $\mathcal{L}_{\text{int}} = 10$ ab^{-1} collider and for a $\sqrt{s} = 3$ TeV and $\mathcal{L}_{\text{int}} = 1$ ab^{-1} collider in Fig. 13 for various $m_{t\bar{t}}$ ranges using 50 GeV bins.[5] In this figure, background B refers to the prediction from SM, and signal S refers to the deviation from SM value due to δ_{yt}. The fact that the significance primarily comes from the interference term is explicit here by noticing higher significance near the threshold. In both panels, one can notice that the sign of significance near the forward region is opposite to the rest for lower energy ranges. This pattern can also be observed in Fig. 6. The origin of this change of sign in the angular distribution can be attributed to the change of sign for the helicity amplitude $\mathcal{M}_{00,++}$ and $\mathcal{M}_{00,--}$ at $\cos\theta \approx 0.7$ and

---

[5]As different lines correspond to different sizes of the $m_{t\bar{t}}$ energy, we choose to represent the result in such a normalization.
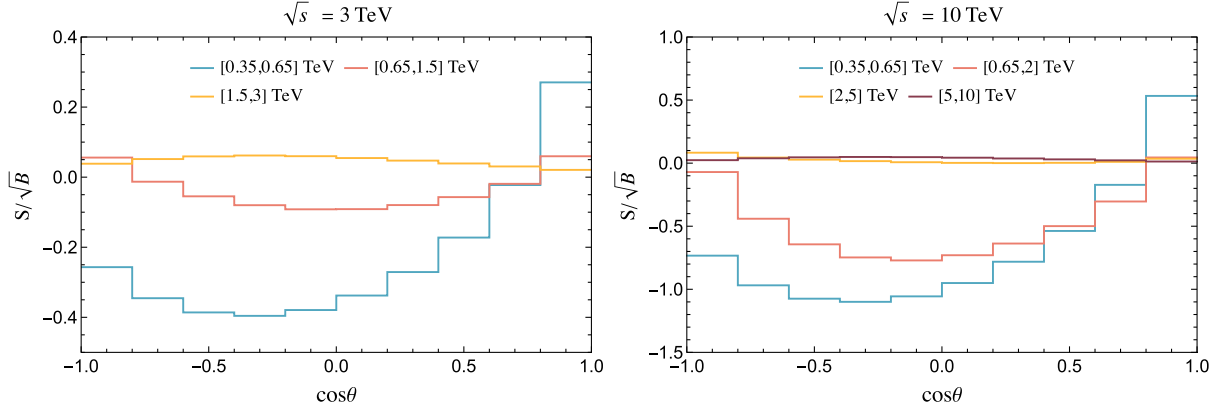
FIG. 13. The significance for 3 TeV (left) and 10 TeV (right) MuC at various ranges of $m_{t\bar{t}}$ as a function of polar angle. We chose $\delta_{yt} = 0.1$ for 3 TeV collider and $\delta_{yt} = 0.015$ for 10 TeV collider which is near the one sigma CL limit for each collider.

$\sqrt{\hat{s}} = 400$ GeV. Since the signal is mostly coming from the interference between the above two channels with the contribution from the Higgs exchange (which has a flat angular dependence), the signal follows the shape of $\mathcal{M}_{00,++}$, $\mathcal{M}_{00,--}$, and this can explain why we observe the pattern in Fig. 13. At higher energies, we have the contribution from the quadratic δ_{yt}^2 term, which is always positive, and so the pattern is not explicit in this region. Another point to note here is that the significance mainly comes from the central bins in angular distribution, so angle cuts in the forward region do not significantly affect our $\Delta\chi^2$ analysis.

APPENDIX C: PARAMETER CONSTRAINTS ON VLQ

The VLQ model modifies the couplings between the top quark and the gauge bosons. The modified Higgs top coupling would make the precision Higgs observable deviate from the SM predictions, such as the Higgs decay modes to diphoton and di-gluon. In SM, the Higgs boson decay into diphoton occurs via the W boson loop and charged fermion loop [57–59], and Higgs decay to di-gluon receives contributions from quark loops [57,60]. Here, we focus on the $h \to gg$ channel since it is more sensitive to the shift s_L^2 and only considers the t and T loop, since the heavy quark dominates this loop-induced coupling. In the VLQ model, we need to consider the T-loop contribution and the

shift in Yukawa couplings for the quark loops. Hence, in total, the amplitude of Higgs to di-gluon mode before QCD correction is

$$\mathcal{M}_q^{\lambda\lambda'ab} = [(1-s_L^2)F_f(\beta_t) + s_L^2 F_f(\beta_T)]$$
$$\times \frac{\alpha_s g(k_1 \cdot k_2 g^{\mu\nu} - k_1^\mu k_2^\nu)\frac{1}{2}\delta^{ab}\epsilon_\mu(k_1)^\lambda \epsilon_\nu(k_2)^{\lambda'}}{2\pi m_W}, \quad \text{(C1)}$$

where

$$\beta_t = \frac{4m_t^2}{m_h^2}, \qquad \beta_T = \frac{4m_T^2}{m_h^2}, \qquad \text{(C2)}$$

$$F_f(\beta) = -2\beta[1 + (1 - \beta)f(\beta)], \qquad \text{(C3)}$$

and

$$f(\beta) = \arcsin^2(\beta^{-\frac{1}{2}}) \quad \text{for } \beta \geq 1. \qquad \text{(C4)}$$

Since the new physics does not change the kinematics, we can compute the excess squared amplitude and constrain the new physics parameters. Using $\delta\Gamma/\Gamma = \delta|\mathcal{M}|^2/|\mathcal{M}_{\text{SM}}|^2$ and inserting the projected precision for the Higgs decay width to di-gluon at future colliders, we can derive the corresponding allowed region in the parameter plane of the VLQ model under consideration.

[1] G. Aad *et al.* (ATLAS Collaboration), Observation of a new particle in the search for the Standard Model Higgs boson with the ATLAS detector at the LHC, Phys. Lett. B **716**, 1 (2012).

[2] S. Chatrchyan *et al.* (CMS Collaboration), Observation of a new boson at a mass of 125 GeV with the CMS experiment at the LHC, Phys. Lett. B **716**, 30 (2012).

[3] M. Boscolo, J.-P. Delahaye, and M. Palmer, The future prospects of muon colliders and neutrino factories, Rev. Accel. Sci. Techol. **10,** 189 (2019).

[4] J. P. Delahaye, M. Diemoz, K. Long, B. Mansoulié, N. Pastrone, L. Rivkin, D. Schulte, A. Skrinsky, and A. Wulzer, Muon colliders, arXiv:1901.06150.

[5] H. Al Ali *et al.*, The muon Smasher's guide, Rep. Prog. Phys. **85,** 084201 (2022).

[6] K. M. Black *et al.*, Muon collider forum report, arXiv:2209.01318.

[7] M. Narain *et al.*, The future of US particle physics—the snowmass 2021 energy frontier report, arXiv:2211.11084.

[8] T. Bose *et al.*, Report of the topical group on physics beyond the standard model at energy frontier for snowmass 2021, arXiv:2209.13128.

[9] C. Aime *et al.*, Muon collider physics summary, arXiv:2203.07256.

[10] D. Schulte, The muon collider, in *Proceedings of the 13th International Particle Accelerator Conference, IPAC'22* (JACoW Publishing, Geneva, Switzerland, 2022), pp. 821–826, https://jacow.org/ipac2022/papers/tuizsp2.pdf.

[11] F. Zimmermann, Accelerator technology and beam physics of future colliders, Front. Phys. **10,** 888395 (2022).

[12] J. de Blas, J. Gu, and Z. Liu, Higgs boson precision measurements at a 125 GeV muon collider, Phys. Rev. D **106,** 073007 (2022).

[13] M. Forslund and P. Meade, High precision higgs from high energy muon colliders, J. High Energy Phys. 08 (2022) 185.

[14] M. Forslund and P. Meade, Precision Higgs width and couplings with a high energy muon collider, arXiv:2308.02633.

[15] A. M. Sirunyan *et al.* (CMS Collaboration), Measurement of the top quark Yukawa coupling from $t\bar{t}$ kinematic distributions in the dilepton final state in proton-proton collisions at $\sqrt{s} = 13$ TeV, Phys. Rev. D **102,** 092013 (2020).

[16] G. L. Kane, W. W. Repko, and W. B. Rolnick, The effective $W^{\pm}$, Z^0 approximation for high-energy collisions, Phys. Lett. **148B,** 367 (1984).

[17] A. Costantini, F. De Lillo, F. Maltoni, L. Mantani, O. Mattelaer, R. Ruiz, and X. Zhao, Vector boson fusion at multi-TeV muon colliders, J. High Energy Phys. 09 (2020) 080.

[18] T. Han, Y. Ma, and K. Xie, High energy leptonic collisions and electroweak parton distribution functions, Phys. Rev. D **103,** L031301 (2021).

[19] T. Han, Y. Ma, and K. Xie, Quark and gluon contents of a lepton at high energies, J. High Energy Phys. 02 (2022) 154.

[20] F. Garosi, D. Marzocca, and S. Trifinopoulos, LePDF: Standard model PDFs for high-energy lepton colliders, J. High Energy Phys. 09 (**2023**) 107.

[21] Y. Ma, Electroweak and Higgs physics at high energies, Ph.D. thesis, University of Pittsburgh (main), 2022.

[22] B. Fornal, A. V. Manohar, and W. J. Waalewijn, Electroweak gauge boson parton distribution functions, J. High Energy Phys. 05 (2018) 106.

[23] V. D. Barger, K.-m. Cheung, T. Han, and R. J. N. Phillips, Probing strongly interacting electroweak dynamics through W^+W^-/ZZ ratios at future e^+e^- colliders, Phys. Rev. D **52,** 3815 (1995).

[24] J. Bagger, V. D. Barger, K.-m. Cheung, J. F. Gunion, T. Han, G. A. Ladinsky, R. Rosenfeld, and C. P. Yuan, The strongly interacting WW system: Gold plated modes, Phys. Rev. D **49,** 1246 (1994).

[25] T. Han, Strong WW scattering physics: A comparative study for the LHC, NLC and a muon collider, in *Proceedings of the Ringberg Workshop: The Higgs Puzzle—What Can We Learn from LEP2, LHC, NLC, and FMC?* (1997), pp. 197–206, arXiv:hep-ph/9704215.

[26] F. Larios, T. M. P. Tait, and C. P. Yuan, Anomalous $W^+W^-t\bar{t}$ couplings at the e^+e^- linear collider, Phys. Rev. D **57,** 3106 (1998).

[27] F. Larios, E. Malkawi, and C. P. Yuan, Probing the electroweak symmetry breaking sector with the top quark, in *Proceedings of the CCAST Workshop on Physics at TeV Energy Scale* (1997), arXiv:hep-ph/9704288.

[28] B. Grzadkowski, M. Iskrzynski, M. Misiak, and J. Rosiek, Dimension-six terms in the standard model Lagrangian, J. High Energy Phys. 10 (**2010**) 085.

[29] E. E. Jenkins, A. V. Manohar, and M. Trott, Renormalization group evolution of the standard model dimension six operators I: Formalism and lambda dependence, J. High Energy Phys. 10 (2013) 087.

[30] I. Brivio and M. Trott, The standard model as an effective field theory, Phys. Rep. **793,** 1 (2019).

[31] B. Henning, X. Lu, and H. Murayama, How to use the standard model effective field theory, J. High Energy Phys. 01 (2016) 023.

[32] B. Henning, X. Lu, and H. Murayama, One-loop matching and running with covariant derivative expansion, J. High Energy Phys. 01 (2018) 123.

[33] J. A. Aguilar-Saavedra, R. Benbrik, S. Heinemeyer, and M. Pérez-Victoria, Handbook of vectorlike quarks: Mixing and single production, Phys. Rev. D **88,** 094010 (2013).

[34] S. A. R. Ellis, R. M. Godbole, S. Gopalakrishna, and J. D. Wells, Survey of vector-like fermion extensions of the standard model and their phenomenological implications, J. High Energy Phys. 09 (2014) 130.

[35] J. M. Alves, G. C. Branco, A. L. Cherchiglia, C. C. Nishi, J. T. Penedo, P. M. F. Pereira, M. N. Rebelo, and J. I. Silva-Marcos, Vector-like singlet quarks: A roadmap, Phys. Rep. **1057,** 1 (2024).

[36] V. Peralta, Phenomenology of vector-like fermions in physics beyond the standard model, Ph.D. thesis, Sao Paulo University, 2017, arXiv:1712.06193.

[37] J. Chen, T. Han, and B. Tweedie, Electroweak splitting functions and high energy showering, J. High Energy Phys. 11 (2017) 093.

[38] C. W. Bauer, N. Ferland, and B. R. Webber, Standard model parton distributions at very high energies, J. High Energy Phys. 08 (2017) 036.

[39] M. Ciafaloni, P. Ciafaloni, and D. Comelli, Bloch-Nordsieck violation in spontaneously broken Abelian theories, Phys. Rev. Lett. **87,** 211802 (2001).

[40] V. Shtabovenko, R. Mertig, and F. Orellana, FeynCalc 9.3: New features and improvements, Comput. Phys. Commun. **256,** 107478 (2020).

[41] J. Alwall, R. Frederix, S. Frixione, V. Hirschi, F. Maltoni, O. Mattelaer, H. S. Shao, T. Stelzer, P. Torrielli, and M. Zaro, The automated computation of tree-level and

next-to-leading order differential cross sections, and their matching to parton shower simulations, J. High Energy Phys. 07 (2014) 079.

[42] R. Ruiz, A. Costantini, F. Maltoni, and O. Mattelaer, The effective vector boson approximation in high-energy muon collisions, J. High Energy Phys. 06 (2022) 114.

[43] P. A. Zyla *et al.* (Particle Data Group), Review of particle physics, Prog. Theor. Exp. Phys. **2020**, 083C01 (2020).

[44] R. L. Workman *et al.* (Particle Data Group), Review of particle physics, Prog. Theor. Exp. Phys. **2022**, 083C01 (2022).

[45] M. Chen and D. Liu, Top Yukawa coupling at the muon collider, arXiv:2212.11067.

[46] T. Han, Z. Liu, and J. Sayre, Potential precision on Higgs couplings and total width at the ILC, Phys. Rev. D **89**, 113006 (2014).

[47] D. M. Asner *et al.*, ILC Higgs white paper, in *Snowmass 2013: Snowmass on the Mississippi* (2013), arXiv:1310 .0763.

[48] M. Ahmad *et al.*, CEPC-SPPC preliminary conceptual design report. 1. Physics and detector, Report No. IHEP-CEPC-DR-2015-01, IHEP-TH-2015-01, IHEP-EP-2015-01.

[49] J. de Blas *et al.*, Higgs boson studies at future particle colliders, J. High Energy Phys. 01 (2020) 139.

[50] M. Negrini (ATLAS and CMS Collaborations), Recent measurements of the top-quark mass and Yukawa coupling using the ATLAS and CMS detectors at the LHC, Proc. Sci. EPS-HEP2021 (**2022**) 479.

[51] M. Cepeda *et al.*, Report from working group 2: Higgs physics at the HL-LHC and HE-LHC, CERN Yellow Rep. Monogr. **7,** 221 (2019).

[52] T. Price, P. Roloff, J. Strube, and T. Tanabe, Full simulation study of the top Yukawa coupling at the ILC at $\sqrt{s} = 1$ TeV, Eur. Phys. J. C **75**, 309 (2015).

[53] A. Aryshev *et al.* (ILC International Development Team), The international linear collider: Report to snowmass 2021, arXiv:2203.07622.

[54] H. Abramowicz *et al.* (CLICdp Collaboration), Top-quark physics at the CLIC electron-positron linear collider, J. High Energy Phys. 11 (2019) 003.

[55] A. Abada *et al.* (FCC Collaboration), FCC physics opportunities: Future circular collider conceptual design report volume 1, Eur. Phys. J. C **79**, 474 (2019).

[56] Z. Liu, K.-F. Lyu, I. Mahbub (2023), https://github.com/ ZhenLiuPhys/WWtt-MuC.

[57] J. R. Ellis, M. K. Gaillard, and D. V. Nanopoulos, A phenomenological profile of the Higgs boson, Nucl. Phys. **B106**, 292 (1976).

[58] M. A. Shifman, A. I. Vainshtein, M. B. Voloshin, and V. I. Zakharov, Low-energy theorems for Higgs boson couplings to photons, Sov. J. Nucl. Phys. **30**, 711 (1979).

[59] W. J. Marciano, C. Zhang, and S. Willenbrock, Higgs decay to two photons, Phys. Rev. D **85**, 013002 (2012).

[60] H. M. Georgi, S. L. Glashow, M. E. Machacek, and D. V. Nanopoulos, Higgs bosons from two gluon annihilation in proton proton collisions, Phys. Rev. Lett. **40**, 692 (1978).